2024

Development of a continuum damage constitutive model and simulation for brittle materials in space infrastructure application

Luis Eduardo Deganis

DEVELOPMENT OF A CONTINUUM DAMAGE CONSTITUTIVE MODEL AND SIMULATION FOR BRITTLE MATERIALS IN SPACE INFRASTRUCTURE APPLICATION

Luis Eduardo Deganis

A DISSERTATION

Submitted in partial fulfillment of the requirements
for the degree of Doctor of Philosophy
in
The Department of Mechanical and Aerospace Engineering
to
The Graduate School
of
The University of Alabama in Huntsville
May 2024

Approved by:

Dr. Gang Wang, Research Advisor
Dr. Kader Frendi, Committee Member
Dr. Judy Schneider, Committee Member
Dr. Jason Mayeur, Committee Member
Dr. Dongsheng Wu, Committee Member
Dr. George Nelson, Department Chair
Dr. Shankar Mahalingam, College Dean
Dr. Jon Hakkila, Graduate Dean

Abstract

DEVELOPMENT OF A CONTINUUM DAMAGE CONSTITUTIVE MODEL AND SIMULATION FOR BRITTLE MATERIALS IN SPACE INFRASTRUCTURE APPLICATION

Luis Eduardo Deganis

A dissertation submitted in partial fulfillment of the requirements for the degree of Doctor of Philosophy

The Department of Mechanical and Aerospace Engineering

The University of Alabama in Huntsville
May 2024

The purpose of this work is to develop a continuum damage constitutive material model and apply it to structural response characterization of brittle materials for *in-situ* construction of space infrastructure. This research improves and expands the utility of the physics-based dominant crack algorithm (DCA) model in order to account for very low-strain rate phenomena in plain concrete structures. The DCA model is strain-rate dependent and has been effectively utilized for highly dynamic phenomena. The model has a strong basis in micromechanics and is able to capture the strain-softening response of brittle materials. The newly developed constitutive model can be easily implemented into a finite element analysis (FEA) platform to predict structural response. Simulation results show good correlation to plain concrete experimental data throughout the material response, including the full softening phase at quasi-static load conditions, and demonstrate the applicability of the model for the intended use. Plain concrete represents a comparable terrestrial construction material and serves as a good proxy to examine the validity of the

model. Current research will benefit a growing research field of space habitat construction techniques with *in-situ* materials through additive manufacturing. The full characterization of material behavior is of vital importance for the structural integrity assessment of habitats and infrastructure that will assure human survival under very challenging environments, isolated in space and time from Earth.

Acknowledgements

Being able to complete my Doctoral research was beyond my reach for a long time, and it would have been impossible without the support and sacrifice of several people.

First, I would like to thank my Research Advisor, Dr. G. Wang, for his guidance and patience. He was able to navigate this ship through the long journey and bring it to its destination. This outcome was in doubt for a while, and I truly appreciate his commitment to see this through to the end.

Second, I would like to thank the other members of my committee, Dr. K. Frendi, Dr. J. Schneider, Dr. J. Mayeur and Dr. D. Wu, for their assistance and comments.

I would also like to express my gratitude to Martin Gardner, who in 2002 gave me the opportunity to emigrate to this wonderful country and allowed for all that came after, a career, a love, a family and now this work.

Sikorsky, a Lockheed Martin Company, has provided me with the financial means to attend and complete my Ph.D. I would like to thank Jon Scallan and Nick Sostilio for their trust and constant encouragement.

I also want to thank my parents, Eduardo and Vilma, for believing in my potential and for pushing me to fulfill it. They have provided a lifelong compass by being an example of dignity and sacrifice. My mom is no longer with us, and I regret deeply that this work was not finished before she passed. *Mami, te extraño. Espero que estés orgullosa.*

I would also like to acknowledge my three sons, Victor, Antonio and Marcos. Spending more time with you and providing my undivided attention while you are still in our home fueled my motivation to finish.

Finally, I would like to dedicate this dissertation to my wife, Kathy, and recognize her graceful command of our home and her kind care for the aspects of our life that were subordinated to this effort. This work would not have been possible if not for her unwavering support and loving understanding. Her patience is boundless, and I needed all of it. We finished, *mi vida*.

Table of Contents

List of Figures

List of Tables

List of Symbols

Symbol	Description
α	Exponential Factor
β^e	Material Constant
β	Newmark-β Constant
c	Wave Speed
$\overline{c}$	Average Crack Size
$\overline{c}_0$	Initial Crack Size
$\dot{\overline{c}}$	Crack Growth Rate
$\dot{c}_{\max}$	Terminal Speed for Crack Growth
$\mathbf{C}_m$	Compliance Tensor of the Matrix
γ	Effective Surface Energy of the Material
	Newmark-β Constant
d	Projectile Diameter
d_k	Damage Variables
d_v	Quadratic Bulk Modulus
$\mathbf{D}$	Damage Tensor
DCA	Dominant Crack Algorithm (Model)
DCA_MSD	Dominant Crack Algorithm with Matrix Shear Damage (Model)
$\mathbf{E}$	Elasticity Tensor
$\mathbf{E}^0$	Linear Elastic Tensor
E	Young's Modulus
$\boldsymbol{\varepsilon}$	Strain Tensor
$\boldsymbol{\varepsilon}_c$	Strain Tensor due to Crack Growth
$\boldsymbol{\varepsilon}^e$	Elastic Strain Tensor
$\boldsymbol{\varepsilon}_m$	Matrix Strain Tensor

$F(\boldsymbol{\sigma}, \bar{c})$	Damage Function
$F^{\mathbf{n}}(\boldsymbol{\sigma}, \mathbf{n}, \bar{c})$	Griffith Instability Criterion
$g(\boldsymbol{\sigma}, \mathbf{n}, \bar{c})$	Energy Release Rate
G	Shear Modulus of the Matrix
H	Heaviside Function
K	Bulk Modulus of the Matrix
λ, μ	Lame Constants
$\mathbf{n}$	Crack Orientation
$\mathbf{n}^c$	Critical Crack Orientation
N_o	Initial Crack Number Density
$n(c,t)$	Crack Number Density Function
ν	Poisson's Ratio
$\mathbf{P}^+$	Positive Projection Operator
$\mathbf{P}^d$	Deviatoric Projection Operator
$\mathbf{P}^{sp}$	Spherical Projection Operator
$\mathbf{Q}^+$	Positive Spectral Tensor of Stress
ρ	Density
$\sigma_1, \sigma_2, \sigma_3$	Principal Stresses
$\boldsymbol{\sigma}$	Stress Tensor
$\sigma_{cr}(\bar{c})$	Tensile Strength of the Material
σ_m	Mean Stress
σ_n	Normal Component of Stress
u	Node Displacement
$\dot{u}$	Node Velocity
$\ddot{u}$	Node Acceleration

Perseverance is not a long race; it is many short races one after the other.

Walter Elliot

Chapter 1. Introduction

1.1 Background

Humanity may be on the verge of the interplanetary colonization era in this century. It is believed that in the next few decades, temporary and permanent human colonies could inhabit Earth's moon and Mars [30]. These colonies will require appropriate habitat arrangements to assure their survival. These habitats will not only provide an air rich pressurized environment that would allow them to breath and possibly farm, but they will also provide shielding from meteorites and outer space radiation [1].

The use of concrete on Earth has proven effective and efficient for infrastructure development. A similar approach is being considered for extraterrestrial applications while taking advantage of *in-situ* materials such as Martian soil or regolith. This is due to the incredible technical challenges and costs associated [7] with interplanetary transportation of Earth's building materials. This technology is referred to as *in-situ* resource utilization (ISRU)

On the other hand, the utilization of *in-situ* materials from such remote locations comes with its own set of challenges such as:

- Full understanding of their composition
- Full understanding of the environment where they will be utilized [2]
- Accurate prediction of their behavior

- Technological maturity and reliability of novel infrastructure construction techniques needed
- Energetic requirements and availability that would allow for *in-situ* developments of structural components

Although further exploration of each of these challenges is presented in the following sections, the main focus of this work is the prediction of structural response of future infrastructure. This work proposes a strain rate dependent damage model for brittle materials that would serve that purpose and could be tuned to reflect *in-situ* material composition as needed.

1.2 Mars Environmental Conditions

Mars is the fourth planet from the Sun, and has two small moons: Phobos and Deimos which most scientists believe are captured asteroids. The average distance from Earth is 225 million km and it is the most accessible planet from Earth. It has caused fascination for decades, with research probes being launched since 1960. Aside from Earth, Mars is the most studied planet.

Since the rotation period of Mars and the tilt of the rotational axis relative to the ecliptic plane are similar to Earth, its days and seasons are comparable to those of Earth [8]. This characteristic combined with Mars' topography and landforms have driven exploration efforts and even plans for Martian colonization.

Other conditions are very different from Earth. Mars has a thin atmosphere that is 95% carbon dioxide; and gravity is about 38% of that on Earth.

The distance between Mars and the Sun is around 1.5 times the distance between the Sun and Earth; which creates conditions where the average temperature on the surface of Mars is -63 °C with a maximum daily temperature difference of 60 °C [9]

Due to its thin atmosphere, harsh conditions such as galactic cosmic radiation (GCR) and micrometeorites, impacts are of concern. Mars also features dust storms and strong winds of up to 30 m/s (100 ft./s). Lastly, Mars also experiences marsquakes.

Studies in the past decades have demonstrated the existence of water on Mars and observations have revealed numerous channel morphologies and traces of river erosion on Mars' surface [20]

In 2002, Odyssey, launched by the U.S. in 2001, firstly discovered that there could be ice in the near-surface layers of Mars. In 2004, ESA announced that the "Mars Express" probe had discovered frozen water in the south pole of Mars.

As can be expected, the environmental conditions presented in this section present challenges (and also opportunities) for future Mars habitat design.

Figure 1.1 Billions of years ago a river flowed across this scene in Mawrth Vallis (Credits: NASA/JPL-Caltech/University of Arizona).

Table 1.1 Comparison of Earth and Martian physical parameters [3].

Property	Earth	Mars
Surface area [km^2]	510.1×10^6	144.9×10^6
Radius [km]	6371	3395
Gravity at Equator [m/s^2]	9.78	3.72
Escape velocity at Equator [km/s]	11.2	5.02
Surface temperature range [ºC]	- 89 to +58	- 143 to +35
Magnetic vector field [A/m]	24 – 56	0
Surface atm pressure [kPa]	101.3	0.4 – 0.87
Day length [Earth days]	1.00	1.02
Sidereal Rotation Time [hr]	23.9345	24.6229

Table 1.2 Comparison of Earth and Martian physical parameters [2][3].

Major atmospheric compositions	Earth (%)	Mars (%)
CO_2	*Minor*	95.1
N_2	78.08	2.59
Ar	*Minor*	1.94
O_2	20.95	0.16
CO	*Minor*	0.06

1.3 Martian Landforms and Geology

Kamps *et al.* (2020) [22] developed a Martian surface global map utilizing compact reconnaissance imaging spectrometer (CRISM) multispectral mapping mode data through clusters method [2]. Figure 1.2 shows the Martian surface as primarily composed of a dust covered region and southern highlands. The main landforms include plains, basins, volcanos, mountains and canyons. Putzig and Mellon (2007) [23] utilized an improved thermal model and discovered duricrusts distributed in mid-latitudes and dust-covered rock, soils with shallow ice distributed in polar regions.

Odyssey discovered that basalt is predominant on the surface of Mars, some of which are rich in olivine [24]. The Mars rover InSight detected Mars is a seismically active planet, but observed marsquakes of magnitude less than 4 mW [25].

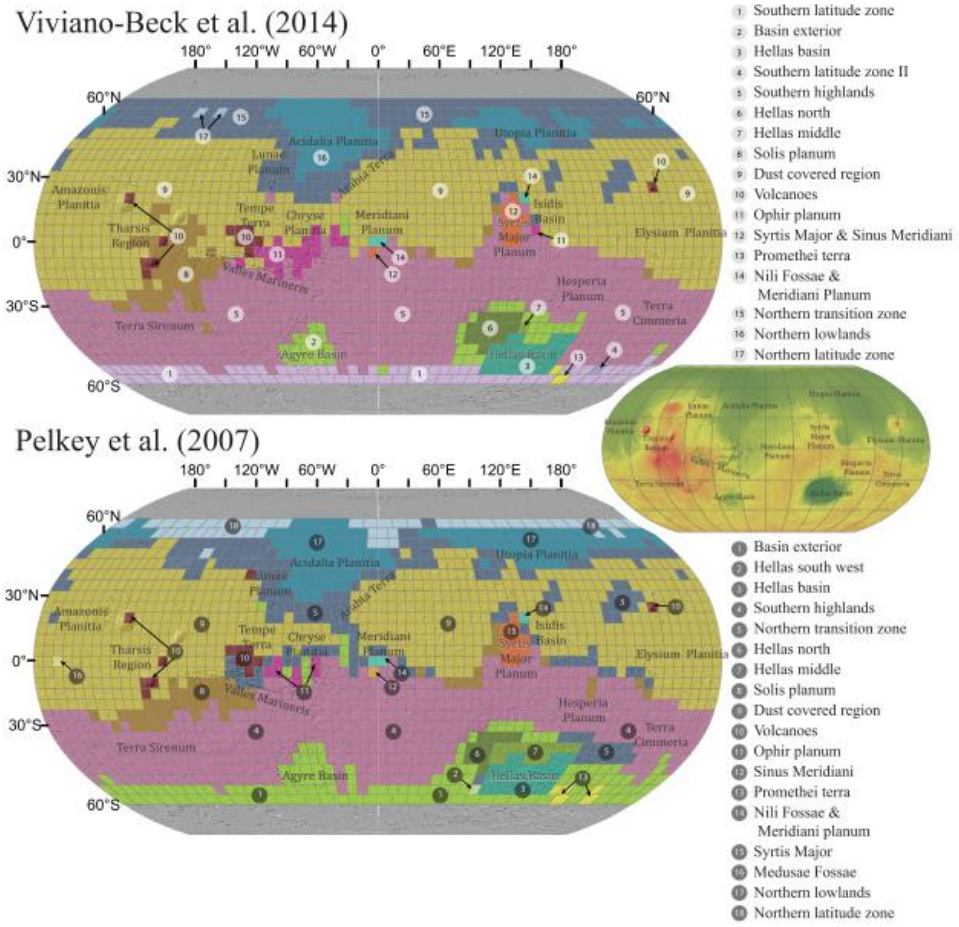

Figure 1.2 Global maps presenting the global surface types based on hierarchical clustering analysis [22].

1.4 Martian Soil (Regolith)

Mars' "soil" consists of surficial unconsolidated fine mineral material and it is usually appropriately defined as regolith, as it is devoid of living matter and very similar to the underlying parent rock [10] (other terms such as aeolian or sediment are also used). On the other hand, regolith is an *in-situ* natural resource that could pave the way for habitat construction on the surface of Mars.

Compounds containing sulfur and calcium elements are widely distributed in Martian surface sediments. The table below lists the main composition of Martian soil,

including suspected magnesium carbonate and amorphous silica. In addition, glassy material or impact glass has also been discovered on Martian soil [20].

To date, no Martian soil samples have returned to Earth, however it has been researched remotely with the assistance of rovers and orbiters.

Table 1.3 Composition of selected Martian soil [11][20][2][3].

Element/ Compound	Viking 1 (Clark *et al.* 1982)	Spirit -Gusev Crater (Gellert *et al.* 2004)	Opportunity – Meridiani Planum (Rieder *et al.* 2004)	Pathfinder – Ares Vallis (Rieder *et al.* 1997)
SiO_2	44	45.8	37.8 - 46.3	62
TiO_2	0.62	0.81	0.7 - 1.3	0.7
Al_2O_3	7.3	10	7.2 - 9.4	10.6
FeO	17.5	15.8	19 - 33.4	12
MgO	6	9.3	6.4 - 7.4	2
CaO	5.7	6.1	5.15 - 7.52	7.3
Na_2O	–	3.3	1.4 - 1.8	2.6
K_2O	< 0.5	0.41	0.37 - 0.49	0.7
SO_3	6.7	5.82	4.52 - 7.29	0
Cl	0.8	0.53	0.33 - 0.47	0.2

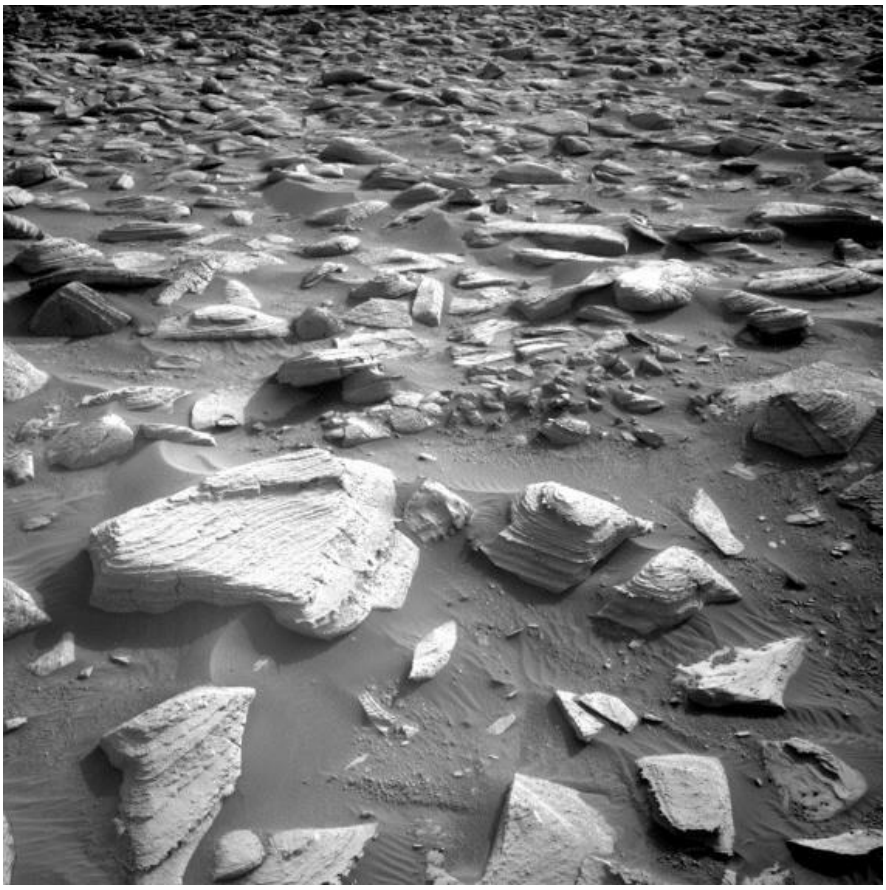

Figure 1.3 Mars surface featuring a layered block with some resistant fin features located on Gediz Vallis ridge - Sol 3948 (Credits: NASA/JPL-Caltech).

Rogers and Christensen [27] categorized the rocks on the surface of Mars into 4 categories: lime-ash basalt rich in high silica glass, pyroxene basalt containing olivine, lime-ash basalt containing olivine and lime-ash basalt using TES [2].

Basalt is a common rock on the surface of Mars and it is formed from the cooling of lava rich in magnesium and iron. Basalt could be widely applied in infrastructure development but requires further characterization to better understand its utility in the Martian environment [2].

Volcanic ash rich in iron is also very prevalent on Mars' surface. It actually gives Mars its characteristic red color as large amount of volcanic ash covered the surface of the

planet in ancient times, and turned red after oxidation. It could be used as a mixing material for cement and an admixture for concrete after grinding. Cement made with volcanic ash is called Pozzolan cement and has relatively small specific gravity compared with Portland cement, lower hydration heat, better corrosion resistance but greater water requirement and shrinkage; and worse frost resistance. It is then well suited for underground projects in humid environments; away from high temperature variation and dry environments [2].

1.5 Martian Soil Simulants

To mitigate the risk of developing infrastructure through ISRU, researchers have been developing "proxies" or simulated Martian soil (simulants), based on data recovered from multiple unmanned exploratory missions.

Table 1.4 Mars Soil Simulants [21][3].

Property replicated	Current Simulants
Chemical/Mineralogical	JEZ-1, JMSS-1, MGS-1, MMS-1 and -2, Y-Mars
Physical/geotechnical	ES-X; KMS-1; MMS Mojave Mars Simulant; UC Mars1; M90
Spectral	JSC Mars-1 and -1A
Magnetic	Salten Skov 1

Figure 1.4 Orbitec (2014) Mars Soil Simulant JSC MARS-1A.

There are mainly two processes to synthesize simulated Martian soil. The whole-rock simulation method identifies and utilizes rocks with similar mineral and chemical composition to source soil. On the other hand, the single mineral simulation method identifies source minerals as the raw materials based on the composition of the source soil. The raw materials are then dried, crushed and screened into different sizes; and then mixed to reflect the source soil composition [2].

1.6 Martian Concrete

The possibility of developing and utilizing concrete in Mars will depend on the *in-situ* material available (including water), the production methods employed and their synthesis energy requirements. Methods for processing and curing concrete are being

researched and proposed for the low-temperature, low-gravity, low-pressure conditions on Mars.

Martian concrete was first proposed in 1996 by McKay *et al.* [26], who postulated that it would be easier to obtain raw materials for concrete on Mars than on the Moon.

At a basic level, concrete is composed of a binder agent and an aggregate. As previously discussed, Martian soil can be used as aggregate. Most binders also need water to form concrete. Water can be condensed or recovered from Mars' ice if necessary, although being such a scarce resource, it is not preferable. Cement is an effective binder solution and is commonly used on Earth. The materials required to produce Martian cement have also been identified in the Martian soil [26].

1.6.1 Martian Binders

NASA started investigating several types of binders in 2006 including sulfur and polymer, and mixed them with regolith in space for additive construction applications [28] that would be suitable for construction under Martian atmospheric pressure and temperature range. As covered before, crushed basalt could be utilized as aggregate. Reches [29] examined potential applicable binders existing on Mars such as plaster of Paris (PoP), ordinary Portland cement (OPC), alkali-activated cement (AAC), geopolymer cement (GC), Mg- and Si-based binder (MSBB), elemental sulfur (ES), and water (by freezing). Those are shown in Figure 1.5 with FA and CA identifying fine aggregate and coarse aggregate respectively.

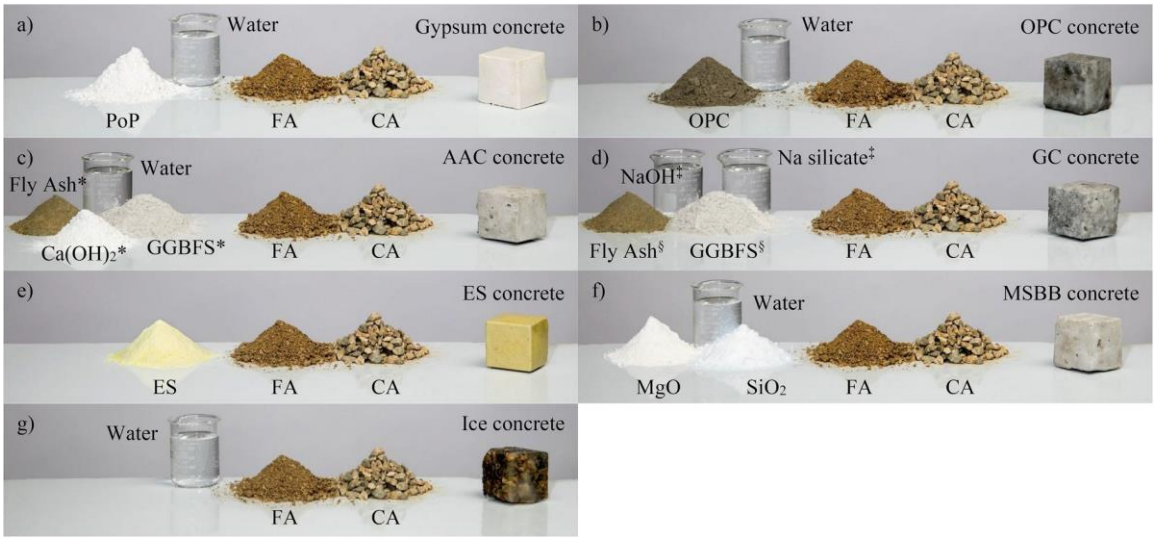

Figure 1.5 Terrestrial concrete formulations with potential applicability on Mars [29].

PoP is a binder typically made from the calcining of gypsum. When mixed with water, it sets and hardens back into solid gypsum. The preparation of PoP with bassanite is of particular interest as it does not require calcining and the availability of bassanite reserves in Mars [29]. The extensive history of terrestrial applications, low energy requirements and fast set/harden are clear advantages for Martian utilization.

Ordinary Portland cement (OPC) and Alkali-activated cement are not preferred due to the scarcity of required raw materials; and high energy requirement of OPC.

Geopolymer cement (GC) is being considered as an alternative for OPC for terrestrial applications. It is made by the combining soluble Alumino-silicate phase (ASPs - *e.g.*, fly ash, GGBFS, or calcined clays) with an aqueous solution of alkali silicate (reaction of silica or an ASP with NaOH or KOH) [29]. GC is very energy efficient as it may require little to no calcining. From a resource stand point, it does not need Ca.

Mg- and Si-based binders (MSBB) are being researched and developed specifically for Mars application and would be synthesized by the reaction of Mg-based olivine (widely available in Mars) with water; although currently is fairly energy intensive.

Elemental Sulfur (ES) is being considered as a binder option [29] for Martian concrete and could be produced from sulfate minerals, which are common on the Martian surface. Furthermore, it features good mechanical and chemical properties (terrestrial applications) and does not require water for mixing and casting, which makes it more preferable. Nevertheless, synthesizing elemental sulfur would be a challenge due to energetic demands. The viability of this binder is dependent on finding sulfur reserves on Mars.

Lastly, water could be used as a binder (with or without aggregates) by casting liquid water and allowing it to freeze solid under the extremely cold Mars conditions. This would be effective for locations where elements are expected to be permanently frozen (e.g., subterranean or near-polar construction) [29].

1.6.2 Martian Aggregates

As previously discussed throughout this document, Martian regolith is a good candidate for a natural aggregate. It is available in a variety of sizes, and could fulfill the need for fine and coarse aggregates. The mechanical properties of regolith are known to be suitable, and a simulant of it has been successfully used on Earth for the manufacture of concrete [29]. On the other hand, *in-situ* use of the aggregate may be influenced by salts in the regolith that could affect the reactivity of the binder. The impact is difficult to predict so aggregates with negligible salt content would be preferred.

1.7 Structural Design Loads Considerations

Habitats and infrastructure in Mars will bare similarities with Earth construction, but will have to respond to specific demands driven by the extraterrestrial environment.

Martian habitat design will have to consider the low gravity environment where the structures will operate, and how that affects static loads driven by gravity. Since structural members would be ~2/3 lighter that on Earth, it presents an opportunity to use comparatively lower strength concrete and/or fewer structural elements. On the other hand, human habitats would need to be pressurized to counteract the thin atmosphere and create a livable environment. This quasi-static load would create a pressure differential (~ 1 atm) and a more critical load condition for a brittle or quasi-brittle concrete structure in tension and bending. Partially or totally burying the structures may help alleviate this concern, at least for some structural members [29], but may not be the preferable solution for long term human habitation due to psychological impact of living underground.

Apart from static loads, transient loads such as wind and seismic loads are present in Mars, although they are probably not as critical as on Earth. The high probability of micrometeorite impacts due to the thin atmosphere is a concern though, and should be taken into consideration when designing infrastructure. Covering structure with regolith may be a possible remediation of the high velocity impact risk [29].

Another consideration is thermal loading and material stability from the extreme cold conditions and temperature fluctuations (low-strain rate loads). This is especially relevant with a thermally conductive material such as concrete; and insulation would be required. As before, burying the structures could be solution.

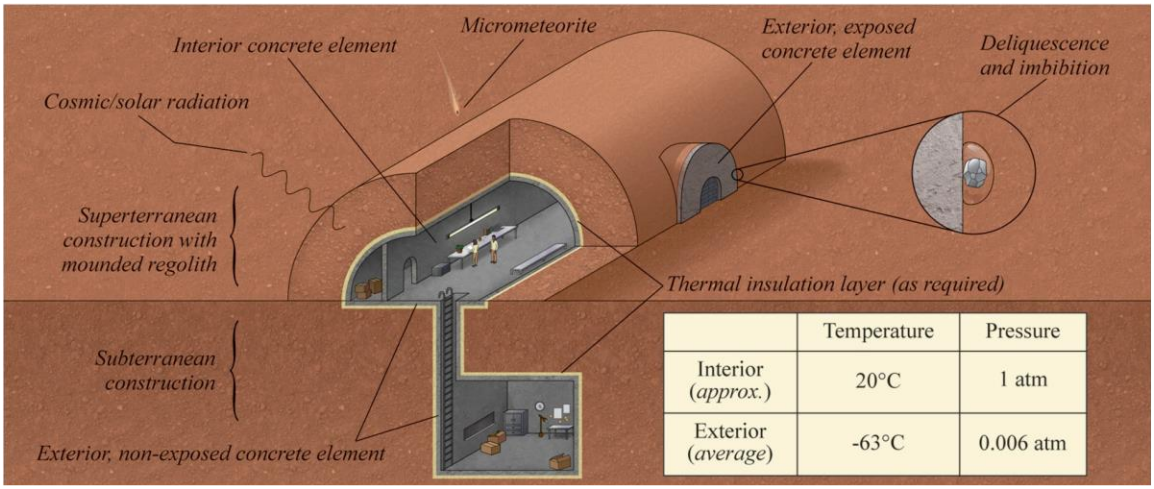

Figure 1.6 Concrete Martian habitats and design requirements [29].

On the other hand, companies such as AI Space factory are concerned with the phycological demands of a Mars mission and the possible detrimental effects of living in a low-lying dome or confined, half-buried structure. Instead, they propose a bright, multi-level, corridor-free habitat that stands upright on the surface of Mars. The construction is a vertically oriented cylinder (4-story habitat) made of poly lactic acid (PLA) bio-polymer reinforced with basalt fiber. The design features a decoupled double shell structure that allows for thermal expansion and contraction of the external shell without affecting the internal shell (and living quarters) [55]. The 3D printed external shell is also the structural member that resists the internal pressure load.

Figure 1.7 MARSHA, AI Space Factory.

Lastly, cosmic and solar radiation is of great concern due to the lack of a magnetosphere and thin atmosphere. Although not directly a strength requirement on the structural design, proper shielding will depend on material selection and also shielding method selected (and how that itself loads the structure, for example by utilizing a thick layer of regolith).

1.8 Possible Construction Approach–Additive Manufacturing

Additive manufacturing (AM) is the technology with most promise for extraterrestrial infrastructure development. Since its first invention in 1970s, it has benefited from significant research efforts that has allowed it to mature, especially during

the last decades. AM or 3D printed components are now found in many industries, including automotive, aerospace and civil construction.

The technology will have to adapt to the extreme environmental conditions on the surface of the Mars, such as ultra-high vacuum, low gravity, freezing temperatures and large temperature difference, and high radiation. In 2014, NASA and Made In Space Inc. (MIS), a US-based company specializing in the development of three-dimensional printers for use in microgravity environments, cooperated to achieve the world's first space 3D printing [2]

ISRU technology will constrain material selection and their properties will determine the manufacturing methods' feasibility, such as the printability, pumpability, buildability, and open time of the regolith materials [3].

1.9 Motivation

As mentioned before in this document, ISRU technologies necessitate a good understanding of the structural materials behavior. Then, a physics-based constitutive model for brittle materials is imperative for effective construction of space infrastructure through additive manufacturing. The material can take the form of Martian or Lunar concrete; while Terrestrial concrete can be used as a proxy to validate the model's effectiveness.

ISRU technologies is a fertile research topic, and this work could impact current efforts by The National Aeronautics and Space Administration (NASA), European Space Agency (ESA) and others that are exploring extraterrestrial infrastructure construction such as:

- Moon-to Mars Planetary Autonomous Construction Technologies (MMPACT): Develop infrastructure on the lunar surface using lunar regolith-based materials.
- ESA Moon Village: Develop and test methods based on new technologies, such as additive manufacturing, that could potentially make use of locally available resources.
- MARSHA, AI Space Factory: Mars habitat design through *in-situ* resource utilization (ISRU) technologies and additive manufacturing.

This research can also have an impact on Earth applications, such as construction of habitats and infrastructure through additive manufacturing or formed concrete.

1.10 Objectives

This work aims to:

- Develop a brittle/quasi-brittle damage constitutive model.
- Implement the constitutive model into a structure.
- Conduct structural analysis and validate model predictions with experimental data.
- Benefit design of structural health monitoring (SHM) scheme for brittle material structures.

1.11 Approach and Scope of Present Work

To achieve the proposed objectives, the work presented herein follows the approach:

- Improve Dominant Crack Algorithm (DCA) model for brittle materials

This is done by improving the Dominant Crack Algorithm (DCA) model and expanding its use to quasi-brittle materials under very low strain rates. DCA is a physics-based micromechanics damage model that is adaptable to different brittle materials but has never been proven effective or validated for quasi-brittle materials under quasi-static loads. The utilization of DCA is convenient for many reasons, such as efficient integration into Finite Element Models (FEM), physics-based structural predictions that don't require successive tunning/corrections and an implicit algorithm that does not require many steps for very low strain rate phenomena. A detailed literature review on brittle material modeling is discussed in Chapter 2.

- Integrate improved model into FEA platform

This is accomplished by integrating the improved damage model into a Finite Element Analysis (FEA) platform that leads to predictive analysis. In this work, this is done by developing a 1-D FEM (2 rod elements) in MATLAB. The framework of this approach is based on the seminal work by H.L. Schreyer and Z. Chen, 1986 [43]. The constitutive model is reduced to a one-dimensional form for this purpose. The equations of motion are resolved through the Newmark-β integration method.

- Characterize structural responses and conduct validation using experimental data

The FEM is run with material variables that correspond to plain concete and boundary conditions based on pioneering work by V.S Gapalaratnam and S.P. Shah, 1985 [44]. The predicted results and experimental data are then used to validate the model for quasi-static loading conditions.

- Collect physical insights to propose structural health monitoring (SHM) scheme for brittle material structures

In our previous effort, we proposed a damage detection approach by examining elastic wave speeds in a brittle material, which are sensitive to changes in the mean size of distributed microcracks [42]. In other words, measuring the wave speed in the material provides a practical means to infer the damage accrual and consequently its structural health. The current effort will allow us to collect physical insights from the structural responses of brittle materials in order to design an innovative SHM scheme by exploring structural response data.

1.12 Organization

Chapter 1 presents background information that includes motivation for current research, exploration of Mars environment, *in-situ* source material availability and current state of infrastructure development technologies. Chapter 2 provides a discussion on brittle and quasi-brittle materials, including plain concrete and strain-softening response that are foundational to the proper understanding of the constitutive model behavior. It also contains a literature review on relevant material models. Chapter 3 is a review of the DCA model from Zuo *et al.*, 2006, its applicability to the current research effort, advantages and limitations. Chapter 4 introduces the new proposed constitutive material DCA_MSD, based on DCA and describes its structural implementation. Chapter 5 presents the results of the structural analysis of a finite element model that contains the new constitutive model, and its correlation to experimental data based on three (3) data sets. Finally, Chapter 6 covers conclusions from this research and future work.

Chapter 2. Brittle and Quasi-Brittle Materials

2.1 Brief Historical Perspective

Brittle materials are all around us and have been at the service of humanity for millennia. We interact with them daily, ceramics in our dishware and decorations, glass in our windows and cellphones, concrete in our infrastructure, rocks in our jewelry, polymers in every plastic object, silicon in our microchips; and too many more uses to count.

Ceramics is one of the most ancient industries and started once humans discovered that clay could be found in abundance and formed into objects by first mixing with water and then firing. Archeologists have uncovered human-made ceramics that date back as early as 28,000 years BC, during the late Paleolithic period in a small prehistoric settlement near Brno, in the Czech Republic [32]. Xiaohong Wu and colleagues [31] discovered ceramic pottery dating back 20,000 years in the Xianrendong Cave, Jiangxi Province, China.

It is believed that ancient glass manufacture was closely related to pottery making, which flourished in Upper Egypt about 8,000 BC. While firing pottery artifacts, the sand in calcium oxide (CaO) combined with soda and was heated by the pottery kiln. This may have resulted in a colored glaze on the ceramic pot. Experts believe that it was not until 1,500 BC that glass was produced independently of ceramics and fashioned into separate items [32].

Concrete has existed in varying forms for thousands of years too. A concrete floor was discovered in a hut in Israel, dated around 7,000 BC. The concrete was made by burning limestone to produce quicklime, was then then mixed with water and stone and left to set. Knowledge of this lime-based material spread through Egypt and Ancient Greece and was adopted by the Romans around 300 BC. The word “concrete” comes from the Latin ‘concretus’, that means “grown together or compounded” [33]

2.2 Brittle and Quasi-Brittle Material Characteristics

In general terms, brittle materials contain a multitude of microcracks that grow and coalesce under load until failure. Also, they have good compressive strength but relatively poor tensile strength (hence the need to steel rebars in reinforced concrete).

Pure brittle materials fracture without plastic deformation and fairly rapidly; and they absorb relatively low amounts of energy prior to failure. Typically, there will be an audible snap sound when the brittle material breaks. Quasi-brittle materials allow for relatively more energy absorption and inelastic behavior before fracture. In this ‘intermediate” category of fracture, the fracture front is surrounded by a large fracture-process zone (FPZ) in which progressive distributed microcracking or other damage occurs. Quasi-brittle structures cannot be represented by Linear Elastic Fracture Mechanics (LEFM), and nonlinear fracture mechanics framework is needed.

Brittle or quasi-brittle fracture of engineering materials is an active research field, that involves different aspects of the mechanics and physics of fracture. Materials include metal alloys, polymers, composites, rocks, and ceramics. Concrete is a classical example of quasi-brittle materials.

Figure 2.1 Plain Concrete Fracture in Tension [40].

Brittle failure occurs under static, dynamic, thermal and cyclic (fatigue) loading conditions. The material damage process is usually very complex as it involves combined effects of load (type and application), size and geometry of the component, temperature, and environment. Understanding the phenomena tied to the energy dissipation in various forms and the identification of microscopic properties and their interactions with macroscopic variables are very challenging topics.

2.3 Fracture Mechanics Discussion

The intention of the section is to introduce fundamental concepts that aid the discussion put forward later in this document and not to provide a comprehensive coverage of fracture mechanics, which would be a dissertation or book by itself.

In its most basic form, fracture mechanics is a specialty within solid mechanics where the presence of a crack is assumed, and the quantitative relations between the crack length, the material's inherent resistance to crack growth, and the stress at which the crack propagates at high speed to cause structural failure [35].

From a historical perspective, fracture mechanics originated within linear elastic assumptions, or Linear Elastic Fracture Mechanics (LEFM). Its genesis would not have been possible without the pioneering work of Ernst Gustav Kirsch's in the development of a linear elastic solution for stresses around a hole in an infinite plate [37]; and the invention of the stress concentration factor at the end of the 19th century.

$$\sigma_{rr} = \frac{\sigma_\infty}{2}\left(1 - \left(\frac{a}{r}\right)^2\right) + \frac{\sigma_\infty}{2}\left(1 - 4\left(\frac{a}{r}\right)^2 + 3\left(\frac{a}{r}\right)^4\right)\cos 2\theta$$

$$\sigma_{\theta\theta} = \frac{\sigma_\infty}{2}\left(1 + \left(\frac{a}{r}\right)^2\right) - \frac{\sigma_\infty}{2}\left(1 + 3\left(\frac{a}{r}\right)^4\right)\cos 2\theta$$

$$\tau_{r\theta} = -\frac{\sigma_\infty}{2}\left(1 + 2\left(\frac{a}{r}\right)^2 - 3\left(\frac{a}{r}\right)^4\right)\sin 2\theta$$

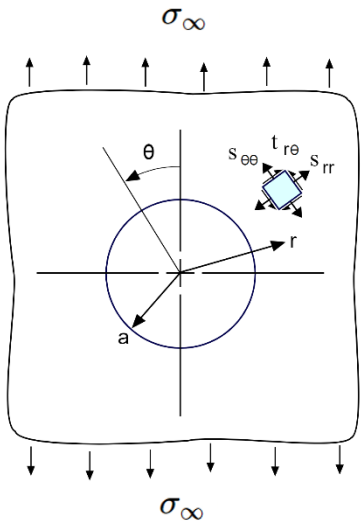

Figure 2.2 Uniaxial Tension - Kirsch's Solution (1898) [36].

At the hole, r = a, and the radial and shear stresses are zero, $\sigma_{rr} = \tau_{r\theta} = 0$ while the hoop stress is maximum for $\theta = \pm 90°$ or $\sigma_{\theta\theta} = 3\,\sigma_\infty$; and the ratio is called the Stress Concentration Factor ($K_t = 3$); and widely used in multiple industries. Of note is the that the stress at the is independent of the size of the hole itself. This is due to the fact that the plate is infinitely large, so the hole's size is inconsequential relative to the plate [35].

It will be obvious to the observer that cracks are not circular or spherical, so this foundational work was modified and expanded by Charles E. Inglis in 1913. He determined the analytical linear elastic solution for the stress field surrounding an ellipse, that at the limit, can be applied to an ellipse flattened to form a crack.

$$\sigma_{max} = \sigma_{\infty}\left(1 + 2\frac{a}{b}\right)$$

or in a more suitable form;

$$\sigma_{max} = \sigma_{\infty}\left(1 + 2\sqrt{\frac{a}{\rho}}\right)$$

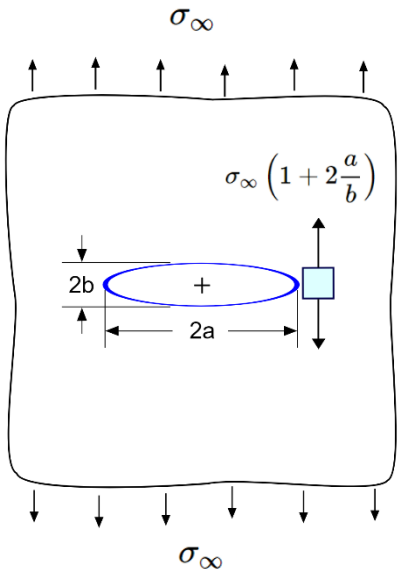

Figure 2.3 Stresses at Elliptical Holes - Inglis's Solution (1913) [36].

Where ρ is the radius of curvature at the tip of an ellipse and is related to its length and width by $\rho = \frac{b^2}{a}$.

Inglis's solution provided two monumental contributions. Firstly, when the radius of curvature at the tip goes to zero (such as in a crack), the max stress at crack tips are predicted to be infinite, even under minimal load. This is not realistic, as no material can withstand infinite stress without experiencing yielding and failure, but it is a tenet of Linear Elastic Fracture Mechanics theory. Secondly, the stress at the tip is proportional to the

square root of the ellipse's width (a) which is markedly different from the stress state at a circular whole (independent of the hole's size).

Although the solution proved controversial and not representative of physical phenomena, it was fundamental in furthering the understanding of crack behavior and became a steppingstone for Griffith's energy-based failure criterion.

Alan Arnold Griffith's developed his seminal work on an energy-based analysis of cracks in 1920 [39]. It is widely considered to be the birth of fracture mechanics. Inspired by Inglis' solution and fully aware of its limitation, he proposed an energy-based approach that bypassed the infinite stress prediction while still making good use of the linear elastic approach. Griffith's approach compared the work required to break atomic bonds to the strain energy released as a crack grows. In short, to break an atomic bond, an amount of work equal to the bond energy must be performed on the system [35].

If we consider the strain energy density, U' (strain energy per unit volume) of a linear elastic material under uniaxial tension as:

$$U' = \frac{\sigma^2}{2E} \tag{2.1}$$

and we consider the Strain Energy Release as the crack grows as

$$U = \frac{\sigma^2}{2E}\, V. \tag{2.2}$$

Griffith's innovation was to compute the strain energy release associated with crack growth for an infinite plate in uniaxial tension; same as Inglis had done a few years before. Griffith used Ingils' case of a flattened ellipse to form a crack and integrated the stress and strain fields to obtain the strain energy as a function of crack length [35]. He obtained the following result for one-half of the infinite plate:

$$U = \frac{\sigma^2}{2E} V - \frac{\sigma^2}{2E} B \pi a^2, \tag{2.3}$$

which is the baseline value (for zero crack length) and a term that progressively reduces the total value with crack growth (quadratic relationship).

If we also consider a crack growing in a solid to a length "a", that has broken several atomic bonds along the way, each requiring a certain amount of work to overcome the atomic bond energy. The total energy (work) can be expressed as

$$E_{bond} = 2\gamma_s a B, \tag{2.4}$$

where γ_s represents the energy required to break atomic bonds per unit surface area created by the crack; $a B$ is the surface area where a is the crack length and B is the part thickness, and two (2) is needed to account for both free surfaces of the crack.

Then, combining both expressions, the total energy of the system is:

$$E_{total} = 2\gamma_s a B + \frac{\sigma^2}{2E} V - \frac{\sigma^2}{2E} B \pi a^2. \tag{2.5}$$

Consequently, for small crack lengths the crack grows in a stable manner, increasing the total energy and requiring energy input for growth. Nevertheless, at longer crack lengths, further growth leads to a decrease in total energy and the crack can grow in an unstable matter until fracture, without any additional external input. We find this threshold by differentiating the total energy with respect to the crack length and equating it to zero,

$$\sigma_f = \sqrt{\frac{2\gamma_s E}{\pi a}} = \sqrt{\frac{\mathcal{G}_c E}{\pi a}}, \tag{2.6}$$

where $\mathcal{G}_c$ is the Griffith Critical Energy Release Rate. Additionally, it is also convenient to resolve for $\mathcal{G}_c$ to introduce the Stress Intensity Factor (K_c), as done by Irwin in 1957,

$$K_c = \sigma_f \sqrt{\pi a} \tag{2.7}$$

$$\mathcal{G}_c = \frac{{K_c}^2}{E}, \tag{2.8}$$

2.4 Strain Softening

Strain softening is the increase in compliance under increased strain that results in reduction of stress. This phenomenon is seen in brittle and quasi-brittle materials, such as concrete, rocks, soil, ceramics and fiber composites. Strain softening occurs in tension, compression and shear. The materials' brittleness and heterogeneity are considered the causes of strain-softening. The phenomenon's mechanism consists of progressive damage accrual, such as dispersed microcracking, void formation or loss of interparticle contacts [48].

It has been demonstrated that the phenomenon frequently affects finite-size regions of the material, depending on material type [48]. This indicates that strain softening could be modeled through Continuum Damage Mechanics (CDM), where an averaging approach could be employed and micromechanical damage effects are smeared over the softening region.

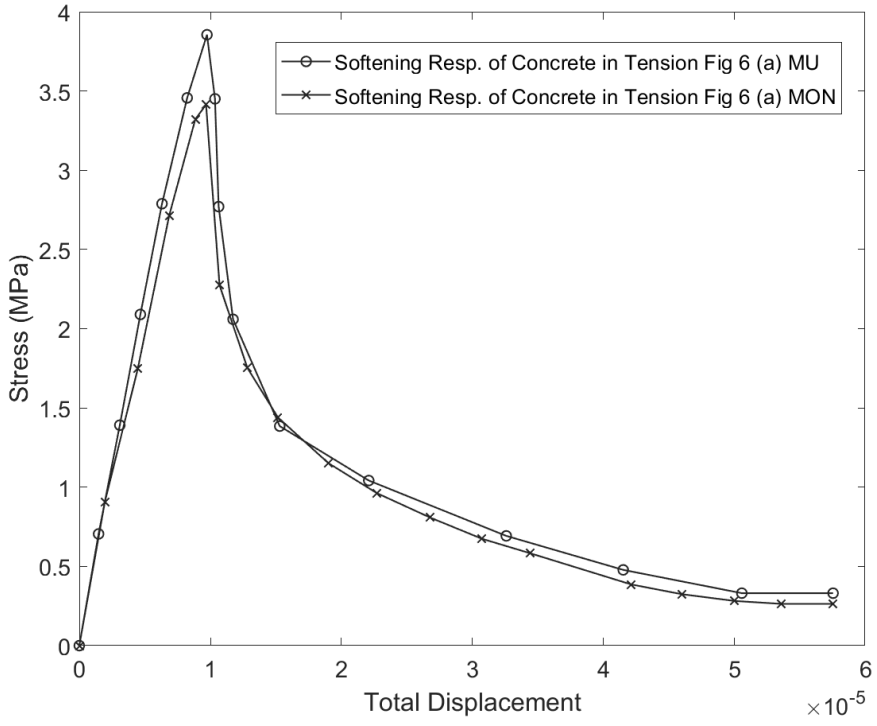

Figure 2.4 Strain Softening Response of Concrete in Tension [44].

2.5 Plain Concrete

Concrete has been the most widely used material for terrestrial infrastructure development for centuries. Plain concrete, also known as plain cement concrete or PCC, is a quasi-brittle material, with high compressive strength and relatively low tensile strength and strain capability. Plain concrete implies that no reinforcement is incorporated into the

construction, that would increase its structural capability, especially in tension. The main constituents are cement, aggregates and water. These types of concrete are mainly used in pavement, floors and building components where high tensile strength is not required.

2.6 Material Models Review

Brittle material's response can be studied from two fronts, using a fracture mechanics approach or using a continuum damage mechanics approach.

Fracture mechanics (FM), which came of age during World War II, studies the fracture phenomenon by assuming presence of a single one macroscopic crack (or at most a small number of discrete cracks) and treating it at a macro-continuum level. In this framework, the crack has a well-defined geometry and the surrounding material microstructure is generally ignored, as well as the interaction between the various local microdefects. This approach has yielded many useful results in the analysis of ductile materials and structures. However, its applicability in brittle materials where the damage is the result of a large amount of microcracks, has been limited [50].

On the other hand, Continuum Damage Mechanics (CDM) accounts for defects by using a homogenization concept to describe their growth macroscopically. This allows the study of the response of microdefects while remaining in the framework of continuum mechanics (CM) [50]. Several continuum damage models have been developed to describe the dynamic response of brittle materials and are currently in use. Their approaches range from the primarily phenomenological models to the more accurate micromechanics-based models. The latter often lead to tensorial description of the material responses [13]. In phenomenological models the damage rate equations are postulated from irreversible thermodynamic potentials or using empirical results. The micromechanical models

normally consider a single crack under stress at the microscopic level and then use statistical arguments to study the macroscopic response [13]. An example of the phenomenological approach would be that of Lemaitre and Chaboche, 1990 [50] and more recently Chen and Bu (2016) [52]. Among the micromechanical models, the works of Dienes and coworkers (Dienes, 1978, 1996; Dienes and Margolin, 1980; Dienes *et al.*, 2006), Addessio and Johnson, 1990; Lewis and Schreyer, 1996 are of particular interest for this work [13-18]. More recently, Zuo *et al.* (2006) developed the Dominant Crack Algorithm (DCA) [13], a micromechanical, rate-dependent model for brittle materials under cyclic loading. Very recently, Yao, Xia and Liu (2018) [52] utilized DCA to investigate the influence of thermal damage on the dynamic tensile strength of two mortars. The Particle Swarm Optimization (PSO) method was utilized to obtain optimized values of DCA model parameters. Their work demonstrated adequate correlation up to maximum tensile stress, but did not show full characterization of the strain-softening response.

Although DCA proves robust for low compressive strains, it is inadequate for high velocity impact when the presence of shockwaves becomes relevant. Deganis L. (the author) and Zuo Q. H. improved DCA in 2011 [53], by incorporating porosity and a nonlinear equation of state (EOS). The new model (DCA_NEOS) accounts for shockwaves in the material and broadened the range of the original model to describe the material response during high velocity impact and spall events.

Zuo, Disilvestro and Richter, 2010 [54] also improved DCA by incorporating plastic deformation of the material, where plasticity is considered through additive decomposition of the total strain rate. This approach was utilized for concrete pavement analysis, under cyclic loading, but no correlation was performed [47].

The implementation of an improved constitutive model based on DCA is advantageous for many reasons, such as efficient integration into Finite Element Models (FEM), physics-based structural predictions that don't require successive tunning/corrections and an implicit algorithm that does not require many steps for very low strain rate phenomena. Furthermore, DCA is currently being used for high strain rate phenomena of pure brittle materials such as impact and explosions, and has already been proved effective under those highly dynamic conditions [13] [19] [49]. This renders DCA as a flexible model that can represent various brittle materials and loading conditions (quasi-static and dynamic events). This is particularly useful when researching extraterrestrial *in-situ* materials and usage environments.

Chapter 3. Dominant Crack Algorithm Damage Model Development

3.1 Introduction

Damage of a material refers to the reduction in the stiffness of the material caused by the nucleation, growth and coalescence of defects (microcracks or cavities). Continuum damage mechanics (CDM) is a modeling approach in which damage is incorporated as a feature of the constitutive equation for the material; often damage is considered as a state variable (it can be scalar, vector, or tensor) whose evolution is postulated as a part of model assumption. Continuum damage mechanics (CDM) has proved to be a useful analysis tool to study the behavior of engineering materials undergoing several types of damage including fatigue, ductile damage, and brittle damage.

A basic requirement in applying the CDM framework is the existence of a large number of small defects in the representative volume element (RVE). This condition allows for the statistical homogenization simplification.

The damage evolution in a ceramic starts by increasing the compliance early in the loading process affecting the elastic response and causing a behavior similar to ductility for an elastic-plastic material. A saturation effect of the number of defects per unit volume is usually experienced in brittle materials.

The damage evolution then slows down only to rapidly increase at the end when the damage accumulation is enough to cause complete failure of the material [12]

The following chapter reviews the DCA model to provide an overall understanding of the model, its advantages and limitations.

The DCA model is a continuum damage model developed by Zuo, *et al.* in 2006 [13] based on the concept of the dominant crack. This material model follows the micromechanical approach that considers the behavior of a single defect and studies the macro-mechanical response by the use of statistical arguments. Before delving completely in understanding the model, it is prudent to review two previous models that served as a guide and eventually were used as a platform for the development of DCA.

The works by Dienes, *et al.* [13] led to the development of a micromechanical model known as Statistical Crack Mechanics (SCRAM). This model was conceived with the purpose of studying the dynamic deformation and fragmentation of brittle materials. The SCRAM model usually considers material isotropy as an initial condition, but anisotropy is dealt with by studying the growth of cracks with several orientations (typically 9, but if needed, more orientations can also been considered).

The foundational work by Dienes, *et al.* was followed by Addessio and Johnson [14]. Based on Dienes' theoretical framework they developed the ISOSCM model, which simplified SCRAM to only consider isotropic damage phenomena. Their goal was to be able to study the dynamic behavior of brittle materials under nearly-isotropic stress state, which is the case in high velocity impact of plates.

The two main assumptions of ISOSCM are that the crack distribution remains isotropic during the damage evolution, and that the crack-size distribution can be represented by an exponential function of the crack size. Also, by averaging the strain and instability condition for a single crack over all crack orientations they were able to

formulate the macroscopic crack strains and isotropic damage surface. The latter depends only on the mean crack size, von Mises stress and the pressure (p), and takes two forms depending on the sign of the pressure. The damage surface becomes the Drucker-Prager granular materials' plastic yield surface for compression ($p>0$), while in tension ($p<0$) approaches the Gurson surface. The Gurson surface models damage in a ductile material caused by the growth of voids under tensile stress.

In the ISOSCM model, the damage variable is based on the initial number of cracks' density, which is constant throughout the deformation event, and the mean crack size. Furthermore, the damage evolution is given by an increase in the mean crack size when the stress state is outside the damage surface. ISOSCM was successfully employed in impact modeling of ceramics and proved popular among researchers working on damage modeling due to its basis in micromechanics, numerical efficiency and mathematical simplicity [13]. This is the case for Zuo, *et al.*, 2006, who adopted ISOSCM for their own damage model (DCA) development. Compared with the ISOSCM model, the new model (DCA) has some distinct differences. In DCA the damage surface is obtained by applying the instability condition to the "dominant crack" and not by averaging over all the crack orientations [14]. The extended Griffith instability criterion $F^{\mathbf{n}}(\boldsymbol{\sigma}, \mathbf{n}, \bar{c})$ adopted in the DCA model can be used for open and closed cracks with friction. The "dominant crack" represents the crack with the critical, or most unstable, orientation $(\mathbf{n}^c)$ under the current state of stress. To account for this critical crack orientation, Zuo and Dienes [15][16] determined the most unstable crack orientations for every possible stress state and developed a damage surface based on the applied stress and crack size, $F(\boldsymbol{\sigma}, \bar{c}) = 0$.

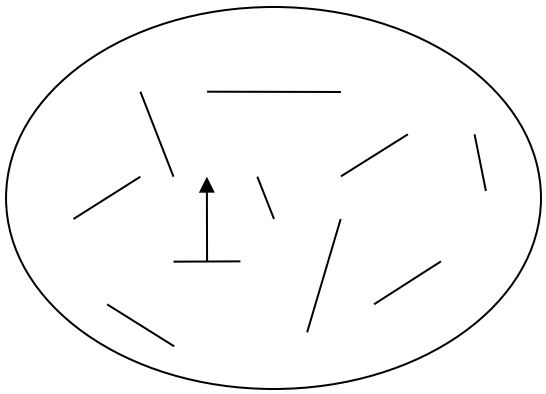

Figure 3.1 DCA Initial Condition.

Among the issues in ISOSCM that were improved in DCA are

1) Discontinuity in the damage surface.
2) Crack-opening strain only dependent on pressure (p) that caused inconsistencies.
3) Lack of physical justification in the damage growth rate exponential function.

The first two issues present thermodynamic inconsistencies under certain cyclic load paths that would allow for energy creation. The DCA model aims at solving these inconsistencies and provides a physical basis for its approach [13].

3.2 DCA Improvements

3.2.1 Continuous Damage Surface

In the ISOSCM model, when the pressure change signs (for example, from compression to tension), the damage surface transforms from the Drucker-Prager type to

that similar to the Gurson surface. This causes a discontinuity in the surface that leads to thermodynamic inconsistency [13].

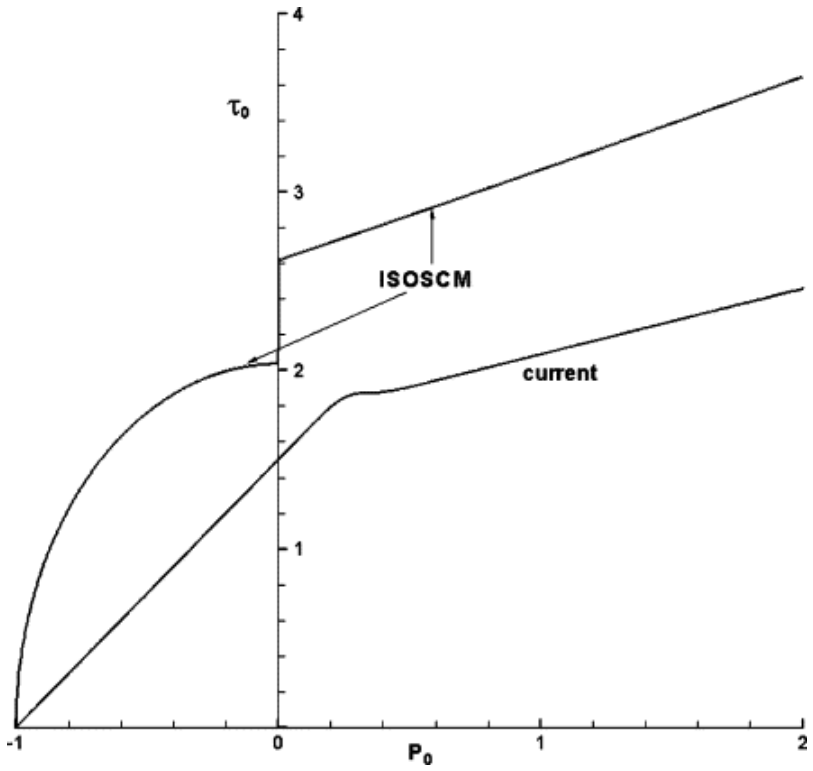

Figure 3.2 Damage Surface Comparison [13].

The damage surface proposed by Zuo, *et al.* (2006) solves the discontinuity and better characterizes brittle behavior. In DCA, the material suffers damage when the crack with average size $(\bar{c})$ becomes unstable in some orientation. This is caused by having a stress value higher than the critical stress for that orientation. Also, the cracks are assumed to be penny-shaped and either open or closed (no partial openings).

As mentioned earlier, the Griffith instability condition is used in DCA and can be expressed in terms of the energy-release rate as

$$F^{\mathbf{n}}(\boldsymbol{\sigma},\mathbf{n},\bar{c}) \equiv \frac{g(\boldsymbol{\sigma},\mathbf{n},\bar{c})}{2\gamma} - 1 \geq 0\,, \tag{3.1}$$

where γ is the effective surface energy of the material (hence 2γ is the critical energy release rate) and $g(\boldsymbol{\sigma},\mathbf{n},\bar{c})$ is the release rate. The energy release rate takes the form:

$$g(\boldsymbol{\sigma},\mathbf{n},\bar{c}) = \frac{f(\boldsymbol{\sigma},\mathbf{n})\bar{c}}{G}\frac{4}{\pi}\frac{(1-\nu)}{(2-\nu)}. \tag{3.2}$$

The stress function $f(\boldsymbol{\sigma},\mathbf{n})$ in the energy release rate depends on the state of the crack (open or closed). If the normal component of traction is tensile $(\sigma_n > 0)$, the crack would be open and the function becomes [13]

$$f(\boldsymbol{\sigma},\mathbf{n}) = \left(1-\frac{\nu}{2}\right)\sigma_n{}^2 + s_n{}^2, \tag{3.3}$$

where the shear (s_n) and normal (σ_n) stresses affect the instability criterion and are defined as

$$\sigma_n = \mathbf{n}\cdot\boldsymbol{\sigma}\mathbf{n}\,, \qquad s_n = \sqrt{\mathbf{n}\cdot\boldsymbol{\sigma}^2\mathbf{n} - \left(\mathbf{n}\cdot\boldsymbol{\sigma}\mathbf{n}\right)^2}\,. \tag{3.4}$$

On the other hand, when the normal component of traction is compressive ($\sigma_n \leq 0$), the crack is closed. Applying the Coulomb friction law, the expression becomes [13]

$$f(\boldsymbol{\sigma}, \mathbf{n}) = \left(s_n + \mu\sigma_n\right)^2 H(s_n + \mu\sigma_n), \tag{3.5}$$

where the static friction coefficient (μ) helps to stabilize the crack [14]. The Heaviside function (H) is one when the argument if positive and zero otherwise.

For a set stress level and crack size, the energy release rate $g(\boldsymbol{\sigma}, \mathbf{n}, \bar{c})$ is maximized at a specific critical orientation $\left(\mathbf{n}^c\right)$ where the crack becomes unstable with the lowest stress. The cracks that show that orientation are the dominant cracks.

Then, for the dominant crack $\mathbf{n} = \mathbf{n}^c$, and

$$F(\boldsymbol{\sigma}, \bar{c}) \equiv F^{\mathbf{n}}(\boldsymbol{\sigma}, \mathbf{n}^c, \bar{c}). \tag{3.6}$$

The damage surface then becomes $F(\boldsymbol{\sigma}, \bar{c}) = 0$, and the material suffers damage and show irreversible deformation when the stress state is outside the damage surface ($F(\boldsymbol{\sigma}, \bar{c}) > 0$). Zuo and Dienes [15][16] determined the critical orientation associated to every stress state possible, and the minimum stress that caused instability. In other words, they found the damage surface for each stress state. Those stress states are

1) Tension (F^{o});
2) Compression (F^{c});
3) Combined opening and shear (F^{os});

4) Pure Shear (F^{ps}).

The forms of each damage surface are briefly discussed in the following sections.

3.2.1.1 Pure Tension Damage Surface $(\sigma_1 \geq \sigma_2 \geq \sigma_3 \geq 0)$

For this stress state, all the cracks are open and the damage surface takes the form of the Rankine maximum tensile criterion for brittle materials:

$$F^t(\boldsymbol{\sigma}, \bar{c}) \equiv \frac{\sigma_1}{S_{cr}(\bar{c}) / \sqrt{1-\nu/2}} - 1 = 0 \tag{3.7}$$

$$S_{cr}(\bar{c}) \equiv \sqrt{\frac{\pi}{2} \frac{2-\nu}{1-\nu} \frac{G\gamma}{\bar{c}}} \,. \tag{3.8}$$

The critical crack has the same orientation of the maximum principal stress, $\mathbf{n}^c = \mathbf{e}_1$.

3.2.1.2 Pure Compression Damage Surface $(0 \geq \sigma_1 \geq \sigma_2 \geq \sigma_3)$

For this stress state, all the cracks are closed and the damage surface takes the form of the Mohr-Coulomb criterion for brittle materials, where the friction helps to stabilize the crack:

$$F^c(\boldsymbol{\sigma}, \bar{c}, \mu) \equiv \frac{\left(\sqrt{\mu^2+1} + \mu\right)\sigma_1 - \left(\sqrt{\mu^2+1} - \mu\right)\sigma_3}{2S_{cr}(\bar{c})} - 1 = 0 \,. \tag{3.9}$$

The critical orientation depends on the friction coefficient, and the angle between the minimum principal stress direction $(\mathbf{e}_3)$ and $\mathbf{n}^c$ can be defined as

$$\theta^c \equiv \tan^{-1}\left(\sqrt{\mu^2+1}+\mu\right). \tag{3.10}$$

3.2.1.3 Combined Tension-Compression Damage Surface $(\sigma_1 > 0, \sigma_3 < 0)$

For this stress state, some cracks are open and others are closed. The form of the damage surface then depends on the relation of magnitudes of the maximum and minimum principal stresses. If $r \equiv \dfrac{\sigma_3}{\sigma_1} < 0$ is the stress biaxiality, then the following stress states can be determined.

3.2.1.3.1 Pure Tension $(-(1-\nu) \le r < 0)$

For this stress state, the damage surface takes the same form as in Section 3.2.1.1 Pure Tension Damage Surface . The critical orientation is also the same.

3.2.1.3.2 Combined Tensile-Shear $(-1 \le r < -(1-\nu))$

For this stress state, the damage surface is elliptical and influenced by all three modes [13]:

$$F^{os}(\boldsymbol{\sigma}, \bar{c}) \equiv \frac{\left(\dfrac{2}{\nu}-1\right)\left(\dfrac{\sigma_1+\sigma_3}{2}\right)^2+\left(\dfrac{\sigma_1-\sigma_3}{2}\right)^2}{S_{cr}^2(\bar{c})}-1=0\,. \tag{3.11}$$

The critical orientation depends on the Poisson's ratio and the stress biaxiality, and the angle between the maximum principal stress $(\mathbf{e}_1)$ and $\mathbf{n}^c$ can be defined as

$$\theta^o = \frac{1}{2}\cos^{-1}\left\{\left(\frac{2}{\nu} - 1\right)\frac{1+r}{1-r}\right\}. \tag{3.12}$$

3.2.1.3.3 Pure Compression $(r < -\left(\sqrt{\mu^2+1} + \mu\right)^2)$

For this stress state, the damage surface takes the same form as in Section 3.2.1.2 Pure Compression Damage Surface $(0 \geq \sigma_1 \geq \sigma_2 \geq \sigma_3)$. The critical orientation is also the same.

3.2.1.3.4 Pure Shear $(-\left(\sqrt{\mu^2+1} + \mu\right)^2 \leq r \leq -1)$

For this stress state $(\sigma_n = 0)$, the damage surface is hyperbolic:

$$F^{ps}(\boldsymbol{\sigma}, \bar{c}) = -\frac{\sigma_1\sigma_3}{S_{cr}^2(\bar{c})} - 1 = 0\,. \tag{3.13}$$

The critical orientation depends on the stress biaxiality, and the angle between the maximum principal stress $(\mathbf{e}_1)$ and $\mathbf{n}^c$ can be defined as

$$\theta^s = \tan^{-1}(1/\sqrt{-r}\,)\,. \tag{3.14}$$

3.2.2 Modified Crack Opening Strain

To understand the concept of crack strain, let us consider a representative volume of the material where there are a large number of small microcracks, randomly orientated and distributed. Under the applied stress, some of the cracks may be opened and others may slide (or be locked if there is enough friction on the crack surfaces), depending on the orientation of the crack and the state of the stress. These "extra," discontinuous displacements over the crack surfaces, when homogenized over a representative volume element (RVE) of the material, are the crack strains, which gives rise to an increase in the compliance of material. For this reason, accurately modeling the crack response is of vital importance in the macroscopic modeling of the material.

The crack number density would be the starting point to study this concept. Empirical research on this subject [13] led to an exponential relation between the crack number density and the crack radius:

$$n(c,\mathbf{n},t) = \frac{N_0(\mathbf{n})}{\bar{c}(\mathbf{n},t)} \exp\left(\frac{-c}{\bar{c}(\mathbf{n},t)} \right). \tag{3.15}$$

In equation (3.15), the initial crack number density $N_0(\mathbf{n})$ depends on the orientation of the crack, and the average crack radius $\bar{c}(\mathbf{n},t)$ evolves with time while also depending on the orientation. The time independence of the initial crack number density assumes that crack nucleation is not present in this model. Addessio and Johnson [14] adopted this concept for the development of ISOSCM with a slight simplification. In the original function, the material anisotropy is dependent on the orientation for both $\bar{c}(\mathbf{n},t)$

and $N_0(\mathbf{n})$. Since ISOSCM only considers isotropic states, that dependence can be overlooked resulting in a simplified version of the function:

$$n(c,t) = \frac{N_0}{\bar{c}(t)} \exp\left(\frac{-c}{\bar{c}(t)}\right). \tag{3.16}$$

This concept is well suited for materials under stress states that are quasi-hydrostatic, like in plate impact. Based on previous works by Dienes, Addessio and Johnson [13] the total crack strain is defined as,

$$\boldsymbol{\varepsilon}_c(\boldsymbol{\sigma},t) = \boldsymbol{\varepsilon}_c^o(\boldsymbol{\sigma},t) + \boldsymbol{\varepsilon}_c^s(\boldsymbol{\sigma},t)\,. \tag{3.17}$$

The total crack strain is then influenced by the opening $(\varepsilon_c^o(\boldsymbol{\sigma},t))$ and shearing $(\varepsilon_c^s(\boldsymbol{\sigma},t))$ of the crack:

$$\boldsymbol{\varepsilon}_c^s(\boldsymbol{\sigma},\bar{c}) = \frac{64\pi}{5G}\frac{1-\nu}{2-\nu} N_0 \bar{c}^3 \boldsymbol{\sigma}^d \tag{3.18}$$

$$\boldsymbol{\varepsilon}_c^o(\boldsymbol{\sigma},\bar{c}) = \frac{64\pi}{15G}(1-\nu) N_0 \bar{c}^3 \left(\boldsymbol{\sigma} + \frac{1}{2} tr(\boldsymbol{\sigma})\mathbf{I}\right) H[-p]\,. \tag{3.19}$$

The Heaviside function in equation (3.19) assures that the crack opening strain only has an influence under tension. This form for the opening crack strain is consistent with crack mechanics when all three principal stresses have the same sign [13]. However, when this is not the case (stresses have mixed signs), the sign of the pressure does not reflect the

crack status (open or closed). Under such a stress state, some cracks are open and some closed, under the same pressure. This problem was solved by Lewis and Schreyer [17][18] who put forward an approximate expression. This expression uses the *activated crack-opening strain*. This computationally efficient approach has its main characteristic in using projection operators to decouple the stress tensor and disregard the compressive stress in the crack opening strain:

$$\boldsymbol{\varepsilon}_c^0(\boldsymbol{\sigma},\bar{c}) = \frac{64\pi}{15G}(1-\upsilon)N_0\bar{c}^3\mathbf{P}^+\left(\mathbf{P}^d + \frac{5}{2}\mathbf{P}^{sp}\right)\mathbf{P}^+\boldsymbol{\sigma}\,. \tag{3.20}$$

The spherical and deviatoric projection operators are defined as $\mathbf{P}^{sp} \equiv \frac{1}{3}(\mathbf{i}\otimes\mathbf{i})$ and $\mathbf{P}^d \equiv \mathbf{I} - \mathbf{P}^{sp}$ respectively. The positive projection operator is defined as

$$\mathbf{P}^+ \equiv \mathbf{Q}^+ \wedge \mathbf{Q}^+\,, \tag{3.21}$$

where $\mathbf{Q}^+$ is a symmetric second order tensor known as the positive spectral tensor of stress as shown below:

$$\mathbf{Q}^+ \equiv \sum_{i=1,3} H[\sigma_i]\mathbf{e}_i \otimes \mathbf{e}_i\,. \tag{3.22}$$

Zuo, *et al.* [13] adopts the same approach for DCA but with a slightly different form for the positive projection operator.

The spectral tensor can be used to define the projected stress, which renders

$$\boldsymbol{\sigma}^{+} \equiv \mathbf{P}^{+}\boldsymbol{\sigma} = \left(\mathbf{Q}^{+} \wedge \mathbf{Q}^{+}\right)\boldsymbol{\sigma} . \tag{3.23}$$

The projector operators and spectral tensor take different values depending on the stress state. This allows for the projected stress to discard the compressive principal components of stress while conserving the tensile ones [13].

The total crack strain in DCA can then be defined as

$$\boldsymbol{\varepsilon}_c(\boldsymbol{\sigma}, \bar{c}) = \beta^e N_0 \bar{c}^3 \left[\frac{3}{2-\upsilon}\boldsymbol{\sigma}^d + \mathbf{P}^{+}\left(\mathbf{P}^d + \frac{5}{2}\mathbf{P}^{sp} \right)\mathbf{P}^{+}\boldsymbol{\sigma} \right] \tag{3.24}$$

$$\beta^e \equiv \frac{64\pi}{15G}(1-\upsilon) . \tag{3.25}$$

3.2.3 Compliance and Damage Tensors

The total strain in a damaged material is the sum of the matrix (crack-free solid) strain and the crack strain:

$$\boldsymbol{\varepsilon} = \boldsymbol{\varepsilon}_m + \boldsymbol{\varepsilon}_c(\boldsymbol{\sigma}, \bar{c}) , \tag{3.26}$$

where the matrix strain is a function of the compliance tensor $(\mathbf{C}_m)$

$$\boldsymbol{\varepsilon}_m = \mathbf{C}_m \boldsymbol{\sigma} \tag{3.27}$$

$$\mathbf{C}_m = \frac{1}{3K}\mathbf{P}^{sp} + \frac{1}{2G}\mathbf{P}^{d} \tag{3.28}$$

$$K \equiv \frac{2G(1+\upsilon)}{3(1-2\upsilon)}. \tag{3.29}$$

Replacing equations (3.27) and (3.24) into (3.26), the total strain can be rewritten as

$$\boldsymbol{\varepsilon} = \mathbf{C}_m \boldsymbol{\sigma} + \beta^e N_0 \bar{c}^3 \left[\frac{3}{2-\upsilon}\boldsymbol{\sigma}^d + \mathbf{P}^{+}\left(\mathbf{P}^d + \frac{5}{2}\mathbf{P}^{sp} \right)\mathbf{P}^{+}\boldsymbol{\sigma} \right]. \tag{3.30}$$

Now, if the damage tensor $\mathbf{D}(\bar{c})$ is defined as an increase in compliance due to damage or crack growth

$$\boldsymbol{\varepsilon}_c(\boldsymbol{\sigma}, \bar{c}) = \mathbf{D}(\bar{c})\boldsymbol{\sigma}, \tag{3.31}$$

the current compliance $\mathbf{C}(\bar{c})$ is dependent on both the elastic effects and damage

$$\mathbf{C}(\bar{c}) = \mathbf{C}_m + \mathbf{D}(\bar{c}), \tag{3.32}$$

and the total strain can be rewritten as

$$\boldsymbol{\varepsilon}(\boldsymbol{\sigma}, \bar{c}) = \mathbf{C}(\bar{c})\boldsymbol{\sigma}. \tag{3.33}$$

The damage tensor would then take the form,

$$\mathbf{D}(\bar{c}) = \beta^e N_0 \bar{c}^3 \left[\frac{3}{2-\upsilon} \mathbf{P}^d + \mathbf{P}^+ \left(\mathbf{P}^d + \frac{5}{2} \mathbf{P}^{sp} \right) \mathbf{P}^+ \right]. \tag{3.34}$$

This robust form of the damage tensor allows for isotropic material response for pure tensile or compressive stress states, while reflecting anisotropic behavior for stress states where the principal stresses have mixed signs.

The evolution of damage variable, defined as $d(\bar{c}) = N_0 \bar{c}^3$, is a useful way to the gauge the damage in the material. This variable is mainly dependent on the mean crack size $(\bar{c})$, since the number density of cracks is a material property that remains constant. Then the damage in the material is governed by the growth of the mean crack size, which depends on the damage surface and damage evolution law. Addessio and Johnson (1990) [14] postulated that $d(\bar{c}) = 2.0$ approximately corresponds to the complete loss of load-carrying capacity or failure of a brittle material.

3.2.4 Modified Damage Evolution Law

One of DCA's main improvements over ISOSCM is its new damage evolution law. Addessio and Johnson [14] use a rate-dependent exponential function for the damage evolution when the stress state is outside the damage surface. Though the exponential function is plausible (it is analogous to the overstress formulation in rate-dependent plasticity) and yields reasonable results, it is not based on physical arguments. Zuo, *et al.* (2006) formulated the damage evolution law using the velocity of crack propagation of the

dominant crack [13]. This approach relates the crack growth law to the applied energy-release rate:

$$\dot{\bar{c}} = \dot{c}_{\max} \left\langle 1 - \frac{2\gamma}{g(\boldsymbol{\sigma}, \mathbf{n}^c, \bar{c})} \right\rangle, \tag{3.35}$$

where the angled bracket is the Macaulay bracket, which takes the value of the argument when positive and zero otherwise.

The terminal speed for crack growth $\dot{c}_{\max}$ depends on the state of the crack with the critical orientation. If the crack is open,

$$\sigma_n(n^c) \equiv \mathbf{n}^c \cdot \boldsymbol{\sigma} \mathbf{n}^c > 0, \tag{3.36}$$

and the terminal speed becomes the *Rayleigh wave speed* C_R. Conversely, if the crack is closed, *i.e.*,

$$\sigma_n(n^c) < 0, \tag{3.37}$$

then the terminal speed takes the value of the *shear wave speed* of the elastic material.

Recalling the Griffith instability condition (3.1), the damage evolution law can be expressed in terms of the damage function:

$$\frac{\dot{\bar{c}}}{\dot{c}_{\max}} = 1 - \frac{1}{1 + \left\langle F\left(\boldsymbol{\sigma}, \bar{c}\right) \right\rangle}. \tag{3.38}$$

It follows from equation (3.38) that the mean crack size grows when the applied stress state is outside the damage surface. Furthermore, the rate of damage accumulation (via crack growth) increases as the distance of the current stress state from the damage surface.

3.3 Numerical Algorithm

Zuo, *et al.* (2006) present two numerical algorithms to solve the constitutive equation

$$\dot{\boldsymbol{\varepsilon}} = \dot{\boldsymbol{\varepsilon}}_m + \dot{\boldsymbol{\varepsilon}}_c = \dot{\boldsymbol{\varepsilon}}_m + (\dot{\boldsymbol{\varepsilon}}_c^d + \dot{\boldsymbol{\varepsilon}}_c^{gr}) = \mathbf{C}_m \dot{\boldsymbol{\sigma}} + \left(\mathbf{D}(\bar{c}) \dot{\boldsymbol{\sigma}} + \frac{\partial \mathbf{D}(\bar{c})}{\partial \bar{c}} \dot{\bar{c}} \boldsymbol{\sigma} \right), \tag{3.39}$$

where the strain rate due to crack growth has two components. One component is elastic and is related to the change in stress rate $(\dot{\boldsymbol{\varepsilon}}_c^d)$, while the other one is inelastic and is caused by damage in the material due to crack growth $(\dot{\boldsymbol{\varepsilon}}_c^{gr})$. The elastic component of the strain rate can be defined as

$$\dot{\boldsymbol{\varepsilon}}_e = \dot{\boldsymbol{\varepsilon}}_m + \dot{\boldsymbol{\varepsilon}}_c^d \,. \tag{3.40}$$

When modeling the material response, the strain rate is usually the input variable and the stress rate is the unknown. Due to this, it is advisable to rewrite the expressions (3.38) and (3.39) in a more useful form as

$$\dot{\boldsymbol{\sigma}} = \left(\mathbf{C}_m + \mathbf{D}(\bar{c}) \right)^{-1} (\dot{\boldsymbol{\varepsilon}} - \dot{\boldsymbol{\varepsilon}}_c^{gr}) = \left(\mathbf{C}_m + \mathbf{D}(\bar{c}) \right)^{-1} \dot{\boldsymbol{\varepsilon}}_c^e \,, \tag{3.41}$$

where

$$\dot{\boldsymbol{\varepsilon}}_c^{gr} = \frac{3\dot{\bar{c}}}{\bar{c}}\mathbf{D}(\bar{c})\boldsymbol{\sigma} \tag{3.42}$$

and

$$\dot{\bar{c}} = \dot{\bar{c}}_{\max}\left(1 - \frac{1}{1+\langle F(\boldsymbol{\sigma},\bar{c})\rangle}\right). \tag{3.43}$$

Equations (3.41) and (3.43) can be integrated numerically using $\Delta t = t^{n+1} - t^n$ as the time step and $\Delta\boldsymbol{\varepsilon} = \dot{\boldsymbol{\varepsilon}}\Delta t$ as the total strain increment. DCA can perform the numerical integrations by means of an implicit algorithm or an explicit one. They both revise the material state after each time step $(\boldsymbol{\sigma}^{n+1}, \bar{c}^{n+1})$, based on the initial state at the beginning of the step $(\boldsymbol{\sigma}^n, \bar{c}^n)$.

The implicit approach requires iterations and is the more complex option. Nevertheless, its convergence proves time step independent and the results remain accurate for larger time steps. Although the implicit algorithm is a more robust general approach, its advantages may not be as relevant for some special cases. When the time step considered is very small due to the nature of the phenomenon, an explicit algorithm may prove the most efficient approach. This is the case for high-rate events such as chemical explosions and high velocity impacts. Furthermore, the explicit algorithm is intrinsically simpler due to the fact that it that does not require iterations. The downside of using this approach is its instability and low accuracy when considering large time steps. This approach is the one followed in ISOSCM while the implicit algorithm is favored by Zuo, *et al.* (2006) for its benchmark calculations in DCA.

The stress at the end of the step $\boldsymbol{\sigma}^{n+1}$ can be determined by using the backward Euler method (implicit) as

$$\boldsymbol{\sigma}^{n+1}(\bar{c}^{n+1}) = \left[\mathbf{I} + 3\left(1 - \frac{\bar{c}^{n1}}{\bar{c}^{n+1}}\right)(\mathbf{C}_m + \mathbf{D})^{-1}\mathbf{D}\right]^{-1}\left[\boldsymbol{\sigma}^n + (\mathbf{C}_m + \mathbf{D})^{-1}\Delta\boldsymbol{\varepsilon}\right]. \tag{3.44}$$

Since the initial stress $\boldsymbol{\sigma}^n$ is carried from the previous time step and the strain increment $\Delta\boldsymbol{\varepsilon}$ is fixed, the only unknown is the final mean crack size $\bar{c}^{n+1}$. In the numerical algorithm, we first check if the step actually involves crack growth. This is done by checking the trial stress against the current damage surface. The trial stress state $\boldsymbol{\sigma}^{tr}$ is the stress in the material if the step is purely elastic (*i.e.*, it does not involve crack growth $(\bar{c}^{n+1} = \bar{c}^n)$):

$$\boldsymbol{\sigma}^{tr} \equiv \boldsymbol{\sigma}^n + \left(\mathbf{C}_m + \mathbf{D}(\bar{c}^n)\right)^{-1}\Delta\boldsymbol{\varepsilon}. \tag{3.45}$$

When the trial and initial stresses are inside or on the damage surface $(F(\boldsymbol{\sigma}^{tr}, \bar{c}^n) \le 0, F(\boldsymbol{\sigma}^n, \bar{c}^n) \le 0)$, the step is elastic and the trial stress is the final stress. If not, the step suffered crack growth and the trial stress does not represent the stress state at the end of the step. For these cases, DCA calculates the final stress using two algorithms depending on the trial stress position with respect damage surface.

If the trial stress is outside the damage surface $(F(\boldsymbol{\sigma}^{tr}, \bar{c}^n) > 0)$, the crack growth becomes

$$\frac{\bar{c}^{n+1}-\bar{c}^{n}}{\dot{c}_{\max}\Delta t}-\left[1-\frac{1}{1+\frac{1}{2}\left(F(\boldsymbol{\sigma}^{n+1},\bar{c}^{n+1})+\left\langle F(\boldsymbol{\sigma}^{n},\bar{c}^{n})\right\rangle\right)}\right]=0\,. \tag{3.46}$$

The final stress $\boldsymbol{\sigma}^{n+1}$ can be calculated using expression (3.44), that only requires $\bar{c}^{n+1}$. This nonlinear system can be solved by an iterative method using the trial state as initial condition. The solution would also be conditioned to be outside the damage surface $(F(\boldsymbol{\sigma}^{n+1},\bar{c}^{n+1})>0)$.

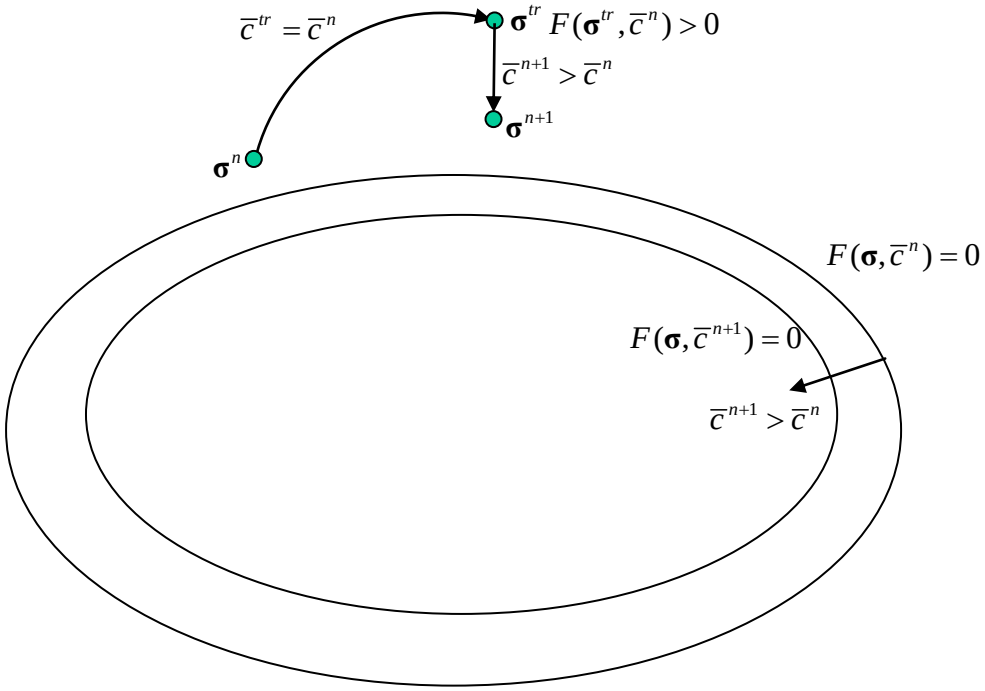

Figure 3.3 Stress Correction Algorithm $F(\boldsymbol{\sigma}^{tr},\bar{c}^{n})>0$.

The second algorithm would cover the case when the trial stress is inside or on the damage surface $(F(\boldsymbol{\sigma}^{tr},\bar{c}^{n})\le 0)$, but the initial state is outside $(F(\boldsymbol{\sigma}^{n},\bar{c}^{n})>0)$. This would imply that there is unloading during the step. In the first moment of the time step, the

material still suffers damage by crack growth (possibly due to inertia) until the diminishing stress reaches the damage surface. From the beginning of the step up to this point, the crack growth decelerates to an equilibrium state. From this point on, the unloading is perfectly elastic [13].

The equilibrium condition is defined by equation (3.43), and points to the complete deceleration of the crack growth when the stress state reaches the damage surface $(F(\boldsymbol{\sigma}^{eq}, \bar{c}^{eq}) = 0)$ at $\Delta t^{eq} < \Delta t$.

By solving equations (3.41)-(3.43) for the new equilibrium sub-step Δt^{eq}

$$\boldsymbol{\sigma}^{eq}(\bar{c}^{eq}, \Delta t^{eq}) = \left[\mathbf{I} + 3\left(1 - \frac{\bar{c}^{n}}{\bar{c}^{eq}}\right)\left(\mathbf{C}_m + \mathbf{D}\right)^{-1}\mathbf{D}\right]^{-1}\left[\boldsymbol{\sigma}^{n} + \Delta t^{eq}\left(\mathbf{C}_m + \mathbf{D}\right)^{-1}\dot{\boldsymbol{\varepsilon}}\right] \tag{3.47}$$

$$\bar{c}^{eq} = \bar{c}^{n} + \left(1 - \frac{1}{1 + \dfrac{F(\boldsymbol{\sigma}^{n}, \bar{c}^{n})}{2}}\right)\dot{\bar{c}}_{\max}\Delta t^{eq} \tag{3.48}$$

$$F(\boldsymbol{\sigma}^{eq}, \bar{c}^{eq}) = 0. \tag{3.49}$$

And rearranging equation (5.48) to get Δt^{eq}, we obtain

$$\Delta t^{eq}(\bar{c}^{eq}) = \frac{\bar{c}^{eq} - \bar{c}^{n}}{\dot{\bar{c}}_{\max}} + \left(1 + \frac{2}{F(\boldsymbol{\sigma}^{n}, \bar{c}^{n})}\right). \tag{3.50}$$

If expression (3.50) is used in (3.47), the $\boldsymbol{\sigma}^{eq}$ reduces to a form only dependent on the crack sized at the equilibrium stress state $\bar{c}^{eq}$. The system can now be solved by a similar algorithm as the one used in equation (3.46).

The remaining of the step does not have inelastic effects and

$$\bar{c}^{n+1} = \bar{c}^{eq} \tag{3.51}$$

$$\boldsymbol{\sigma}^{n+1} = \boldsymbol{\sigma}^{eq} + \left(\mathbf{C}_m + \mathbf{D}(\bar{c}^{n+1})\right)^{-1} \Delta\boldsymbol{\varepsilon}^{e}\,. \tag{3.52}$$

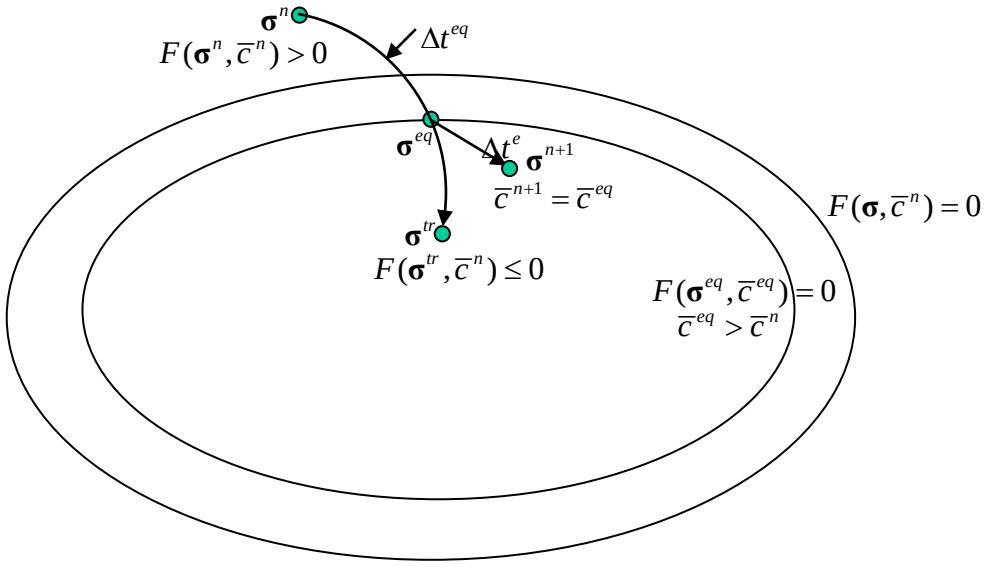

Figure 3.4 Stress Correction Algorithm $F(\boldsymbol{\sigma}^{tr}, \bar{c}^{n}) \le 0$ and $F(\boldsymbol{\sigma}^{n}, \bar{c}^{n}) > 0$.

As previously mentioned, Addessio and Johnson adopt an explicit algorithm to solve the constitutive equations. This approach avoids the use of iterations and calculates

the state of the material at the end of the step based solely on the conditions at the beginning of the step.

Then,

$$\Delta\bar{c} = \dot{c}_{\max}\Delta t\left(1-\frac{1}{1+\left\langle F(\boldsymbol{\sigma}^n,\bar{c}^n)\right\rangle}\right) \tag{3.53}$$

$$\Delta\boldsymbol{\varepsilon}_c^{gr} = \left(\frac{3\Delta\bar{c}}{\bar{c}^n}\right)\mathbf{D}(\bar{c}^n)\boldsymbol{\sigma}^n. \tag{3.54}$$

Equations (3.53) and (3.54) provide the increments necessary to define the state at the end of the step:

$$\bar{c}^{n+1} = \bar{c}^n + \Delta\bar{c} \tag{3.55}$$

$$\boldsymbol{\sigma}^{n+1} = \boldsymbol{\sigma}^n + \left(\mathbf{C}_m + \mathbf{D}(\bar{c}^n)\right)^{-1}\left(\Delta\boldsymbol{\varepsilon}^e - \Delta\boldsymbol{\varepsilon}^{gr}\right). \tag{3.56}$$

3.4 DCA Model Stability and Well-posedness

It is widely recognized that classical continuum models, without an internal length scale, lead to excessive mesh dependence in finite elements simulations when strain-softening models are used, and are unable to reproduce the size effect commonly observed in quasi-brittle failure [56][57][58][59]. Furthermore, damage accrual tends to localize in the smallest band that can be captured by the spatial discretization, which is ultimately set by the size of a single element in the mesh [56]. This strain-softening behavior can cause the Initial-Boundary-Value Problem (IBVP) associated with the model to be

mathematically ill-posed if the model does not take strain-rate or spatially nonlocal effects into account [60][61]. In this case, ill-posedness implies that small differences in initial-boundary conditions can lead to significantly different solutions (even for a finite time) and often results in lack of solution convergence upon mesh refinement.

In the Dominant Crack Algorithm (DCA), the rate-dependent damage evolution law (Eq. 3.28) is analogous to the classical over-stress model frequently used in rate-dependent plasticity [13]. The need for incorporating rate-dependence in plasticity models, especially when material response involve softening and localization, has long been acknowledged [62]. The rate-effects provide a length-scale needed in a well-posed initial/boundary value problem [13]. Kunin and Zuo, 2016 [60] investigated the stability and well-posedness of DCA by examining the behavior of dynamic perturbations to the steady-state solution of uniaxial-stress loading. For a well-posed boundary-value problem, the introduction of perturbations of large wave number (small wave length) due to mesh refinement should not cause the numerical solution to diverge (as the mesh is refined). It was then shown that by incorporating the strain-rate effect in DCA, perturbations of all wave lengths remain bounded for finite times, making the problem well-posed. The research also demonstrated that the corresponding rate independent model was ill-posed, and perturbations grow unbounded with the wave number, even for finite times [60].

Chapter 4. New Constitutive Model and Structural Implementation

4.1 Introduction

This section presents the current modeling effort. It includes the specific implementation of the DCA model for uniaxial loading, the incorporation of a proposed improvement to expand the usage of the model for very low-strain rate phenomena in quasi-brittle materials and finally the application in a simplified finite element model.

The structural implementation is performed in a 1-D FEM, under uniaxial strain (controlled displacement). Then, it consists of:

- Deriving constitutive model for uniaxial tensile loading;
- Reducing the constitutive model to 1-D for to use in rod elements;
- Constructing local and global matrices for FEM;
- Determining model parameters for material and strain-rate of interest;
- Solving the Equation of Motion (ODE).

4.2 DCA for Uniaxial-Strain Loading

Assume a uniaxial strain loading with a constant strain rate: $\boldsymbol{\varepsilon}(t) = \varepsilon_1(t)\mathbf{e}_1 \otimes \mathbf{e}_1$, where $\varepsilon_1(t) = \dot{\varepsilon}_0 t \geq 0$, with $\mathbf{e}_1$ representing the strain direction. The stress tensor becomes $\boldsymbol{\sigma}(t) = \sigma_1(t)\mathbf{e}_1 \otimes \mathbf{e}_1 + \sigma_2(t)\left(\mathbf{e}_2 \otimes \mathbf{e}_2 + \mathbf{e}_3 \otimes \mathbf{e}_3\right)$, where $\sigma_1(t)$ and $\sigma_2(t)$ are, respectively, the axial and transverse stresses, and $\sigma_1(t) > \sigma_2(t) > 0$. This case corresponds to Case B.2 of

Refence [13] for which the positive projection operator becomes the identity tensor, and the damage tensor is isotropic and given by

$$\mathbf{D}(\bar{c}) = \beta^e N_0 \bar{c}^3 \left(\frac{5-\nu}{2-\nu} \mathbf{P}^d + \frac{5}{2} \mathbf{P}^{sp} \right). \tag{4.1}$$

Also, substituting Eqs. (4.1) and (3.28) into Eq. (3.32) returns the compliance tensor of the material:

$$\mathbf{C}(\bar{c}) = \left(\frac{1}{3K} + \frac{5}{2} \beta^e N_0 \bar{c}^3 \right) \mathbf{P}^{sp} + \left(\frac{1}{2G} + \frac{5-\nu}{2-\nu} \beta^e N_0 \bar{c}^3 \right) \mathbf{P}^d . \tag{4.2}$$

The spherical and deviatoric projection operators have previously been defined as $\mathbf{P}^{sp} \equiv \frac{1}{3}(\mathbf{i} \otimes \mathbf{i})$ and $\mathbf{P}^d \equiv \mathbf{I} - \mathbf{P}^{sp}$ respectively, where $\mathbf{P}^{sp}$ and $\mathbf{P}^d$ are orthogonal. Then, the instantaneous elasticity tensor is:

$$\mathbf{E}(\bar{c}) = \mathbf{C}^{-1}(\bar{c}) = 3\hat{K}(\bar{c}) \mathbf{P}^{sp} + 2\hat{G}(\bar{c}) \mathbf{P}^d \tag{4.3}$$

and remains isotropic with reduced moduli, depending on the mean crack size [16]

$$\hat{G}(\bar{c}) = \frac{G}{1 + \gamma_t^e N_0 \bar{c}^3}; \qquad \gamma_t^e \equiv \frac{128\pi}{15} \frac{(5-\nu)(1-\nu)}{2-\nu} \tag{4.4}$$

$$\hat{K}(\bar{c}) = \frac{K}{1+\kappa^e N_0 \bar{c}^3}; \qquad \kappa^e \equiv \frac{64\pi}{3}\frac{1-\nu^2}{1-2\nu}. \tag{4.5}$$

Considering uniaxial strain loading, the stress-strain response becomes [42]

$$\sigma_1 - \sigma_2 = 2\hat{G}\varepsilon_1(t) \tag{4.6}$$

$$\sigma_1 + 2\sigma_2 = 3\hat{K}\varepsilon_1(t), \tag{4.7}$$

and solving for $\sigma_1(t)$ and $\sigma_2(t)$:

$$\sigma_1(t) = \bar{E}(\bar{c})\varepsilon_1(t) \tag{4.8}$$

$$\sigma_2(t) = \Lambda(\bar{c})\varepsilon_1(t) \tag{4.9}$$

where, for convenience, we define the uniaxial-strain modulus $\bar{E}(\bar{c})$ and the Lame constant $\Lambda(\bar{c})$ of the damaged material as

$$\bar{E}(\bar{c}) \equiv \hat{K} + \frac{4}{3}\hat{G} \tag{4.10}$$

$$\Lambda(\bar{c}) \equiv \hat{K} - \frac{2}{3}\hat{G}, \tag{4.11}$$

where $\hat{K}$ and $\hat{G}$ are calculated by Eqs. (4.4)-(4.5). Then, with a strain history input of $\varepsilon_1(t)$, the stress can be determined, when the crack size $\bar{c}(t)$ is calculated.

The damage evolution expression for $F(\boldsymbol{\sigma}, \bar{c})$ under a general stress state were given previously by Eq. (3.38). For uniaxial-strain tension, where the three principal stresses are tensile, the damage surface reduces to that of the Rankine maximum tensile criterion for brittle materials:

$$F(\boldsymbol{\sigma}, \bar{c}) = \frac{\sigma_1}{\sigma_{cr}(\bar{c})} - 1, \qquad \sigma_{cr}(\bar{c}) \equiv \sqrt{\frac{\pi}{1-\nu}\frac{G\gamma}{\bar{c}}}, \tag{4.12}$$

where σ_1 is the largest principal stress, $\sigma_{cr}(\bar{c})$ is the tensile strength of the material, which decreases as the mean crack size $\bar{c}$ grows.

For uniaxial strain loading, a governing equation for $\bar{c}(t)$ is obtained by substituting Eq. (4.12) into (3.38):

$$\dot{\bar{c}} = \dot{c}_{\max}\left(1 - \frac{1}{1 + \left\langle \frac{\sigma_1}{\sigma_{cr}(\bar{c})} - 1 \right\rangle}\right) \tag{4.13}$$

and by resolving $\sigma_1(t)$ in (4.8) and (4.13),

$$\dot{\bar{c}} = \dot{c}_{\max}\left(1 - \frac{1}{1+\left\langle \frac{\bar{E}(\bar{c})\varepsilon_1(t)}{\sigma_{cr}(\bar{c})} - 1 \right\rangle}\right). \tag{4.14}$$

For the constant-rate loading considered, the crack size does not grow when the applied strain is below a limit:

$$\dot{\bar{c}} = 0, \quad \bar{c}(t) = \bar{c}_0; \qquad \text{for} \qquad 0 \le \varepsilon_1(t) \le \varepsilon_{1c}$$

and ε_{1c} is the strain required for crack growth initiation and is determined by $F(\boldsymbol{\sigma}, \bar{c}_0) = 0$

$$\varepsilon_{1c} = \frac{\sigma_{cr}(\bar{c}_0)}{\bar{E}(\bar{c}_0)}. \tag{4.15}$$

For $\varepsilon_1(t) > \varepsilon_{1c}$, then $F(\boldsymbol{\sigma}, \bar{c}) > 0$, and $\dot{\bar{c}} > 0$. The mean crack size $\bar{c}(t)$ is found by solving Eq. (4.14). Due to the nonlinear and complex nature of Eq. (4.13), a numerical solution is employed. Considering a time step of $\Delta t \equiv t^{n+1} - t^n$, let $\bar{c}^n$ be the crack size at the beginning of the step and $\varepsilon_1^{n+1} \equiv \varepsilon_1\left(t^{n+1}\right)$ be the applied axial strain at the end of the step, then an implicit integration of Eq. (36) can be written as

$$f\left(\bar{c}^{n+1}\right) \equiv \frac{\bar{c}^{n+1} - \bar{c}^n}{\dot{c}_{\max}\Delta t} - \left(1 - \frac{\sigma_{cr}(\bar{c}^{n+1})}{\bar{E}(\bar{c}^{n+1})\varepsilon_1^{n+1}}\right) = 0, \tag{4.16}$$

where $\bar{c}^{n+1}$ in the nonlinear algebraic equation can be calculated by Newton iteration. A stand-alone MATLAB code has been written which implements the concepts presented above.

4.3 DCA with Matrix Shear Damage (DCA_MSD)

The DCA model is a continuum damage model, grounded in micro-mechanics that provides physics-based predictions, and can be efficiently implemented through implicit algorithms in finite element models. These characteristics make it very appealing for adoption on structural analysis, especially for materials where the material and model variables characterization will be very challenging, such as extraterrestrial applications.

The DCA model has its origins on highly dynamic phenomena of pure brittle materials, such as impact and explosions [13] [19]. It has proved effective under those conditions [49]. Conversely, adequate model correlation at low strain rates of quasi-brittle materials has not been established.

It will be shown later in this document that the current formulation of DCA does not provide adequate correlation through the softening phase of the response for plain concrete under tension at quasi-static loads.

The intention of this work is to expand the utility of the DCA model for very low-strain rate phenomena in plain concrete (Earth, Lunar or Martian concrete). A model improvement is then proposed to better represent the physics under very-low strain rate phenomena of quasi-brittle materials and improve correlation. The model improvement postulates a degradation of the Shear Modulus of the matrix (G) based on the evolution of the mean crack size $\bar{c}(t)$:

$$G(\bar{c}) = f(\bar{c}). \tag{4.17}$$

DCA assumes the material matrix as linear isotropic and G remains constant throughout the deformation event. This decouples the matrix response to crack damage but also implies that the matrix retains shear stiffness more efficiently than the experimental results for very low strain rate of quasi-brittle materials seem to indicate. Additionally, the DCA approach may be more adequate for high strain rate phenomena, like impacts and explosions, when the impulsive input function fights the inertia of the material composition and is not able to fully transfer its impact with the matrix. This is not true for low strain rates, when the inertial effect is negligeable, and the input load or displacement effects have time to distribute its impact though every component of the material. Also, as discussed before, the crack number density is time independent and remains constant throughout the response, retaining its original value (N_0). This is numerically efficient but implies that, not only there is no consideration for crack nucleation and coalescence, but also that the defects in the representative volume element (RVE) being activated by the stress state also remain constant. This again, may not be true for lower strain rates, and material that was considered intact (matrix) during higher strain rate phenomena (contained microcracks that were not active in the response) is now affected. In other words, the total damage is more pervasive than what is currently being captured by DCA.

The current work then proposes a more coupled effect where the crack growth also impacts the matrix material properties through the degradation of the matrix shear modulus (G), which itself affects the crack growth though its effect on K, β^e, σ_{cr}, and ultimately

on E. This approach suggests increased damage and the final stiffness of the system is reduced, matching experimental data more closely.

Going forward, the new constitutive model based on the new hypothesis is referred to as "DCA with Matrix Shear Damage" or DCA_MSD for short.

As a first approach, damage accumulation in G is based on an exponential function of the crack size evolution,

$$G(\bar{c})_j = G(\bar{c})_{j-1}\left(\frac{\bar{c}_{j-1}}{\bar{c}_j}\right)^{\alpha} \tag{4.18}$$

and the exponential factor (α) takes the form shown below based on the adequate experimental correlation (Chapter 5) and efficient numerical implementation:

$$\alpha = \pi\frac{\bar{c}_j}{\bar{c}_0}\,. \tag{4.19}$$

Consequently, the general formulation of DCA is modified as presented below. For clarity, a new variable will be defined as $G_D \equiv G(\bar{c})$, that denotes the new dependency of the shear on the crack evolution for the proposed modification. The total strain in Eq. 4.26 becomes

$$\boldsymbol{\varepsilon} = \boldsymbol{\varepsilon}_m(G_D) + \boldsymbol{\varepsilon}_c(\boldsymbol{\sigma}, \bar{c}, G_D), \tag{4.20}$$

where the matrix is not considered undamaged any longer and,

$$\boldsymbol{\varepsilon}_m(G_D) = \mathbf{C}_m(G_D)\boldsymbol{\sigma}. \tag{4.21}$$

The matrix compliance is now:

$$\mathbf{C}_m(G_D) = \frac{1}{3K(G_D)}\mathbf{P}^{sp} + \frac{1}{2G_D}\mathbf{P}^{d}, \tag{4.22}$$

where the Bulk Modulus (4.29) is now defined as

$$K(G_D) \equiv \frac{2G_D(1+\nu)}{3(1-2\nu)}. \tag{4.23}$$

Furthermore, the damage tensor is also affected (coupled damage), by the effect on β^e. Then (4.31) now becomes

$$\boldsymbol{\varepsilon}_c(\boldsymbol{\sigma}, \bar{c}, G_D) = \mathbf{D}(\bar{c}, G_D)\boldsymbol{\sigma}, \tag{4.24}$$

where

$$\mathbf{D}(\bar{c}, G_D) = \beta^e(G_D)N_0\bar{c}^3\left[\frac{3}{2-\upsilon}\mathbf{P}^{d} + \mathbf{P}^{+}\left(\mathbf{P}^{d} + \frac{5}{2}\mathbf{P}^{sp}\right)\mathbf{P}^{+}\right] \tag{4.25}$$

and β^e is now dependent on the damaged $G(\bar{c})$

$$\beta^e(G_D) \equiv 64\,\pi\,\frac{1-\nu}{15G_D}. \tag{4.26}$$

Finally, the total compliance (3.32) now features the coupled effect and is carried on through the calculation of stress:

$$\mathbf{C}(\bar{c}, G_D) = \mathbf{C}_m(G_D) + \mathbf{D}(\bar{c}, G_D) \tag{4.27}$$

$$\mathbf{E}(\bar{\boldsymbol{c}}, G_D) \equiv \mathbf{C}(\bar{\boldsymbol{c}}, G_D)^{-\mathbf{1}} = \left(\mathbf{C}_{\boldsymbol{m}}(G_D) + \mathbf{D}(\bar{\boldsymbol{c}}, G_D)\right)^{-\mathbf{1}} \tag{4.28}$$

$$\boldsymbol{\sigma} = \mathbf{E}(\bar{c}, G_D)\boldsymbol{\varepsilon}. \tag{4.29}$$

Regarding the damage evolution law, it retains the same format as Eq. (3.38), but the damage surface will be affected.

The same approach and conditions presented for the uniaxial-strain tensile load case in Section 4.2 are valid for the new assumptions, then damage matrix (4.1) becomes

$$\mathbf{D}(\bar{c}, G_D) = \beta^e(G_D) N_0 \bar{c}^3 \left(\frac{5-\nu}{2-\nu}\mathbf{P}^d + \frac{5}{2}\mathbf{P}^{sp}\right) \tag{4.30}$$

and the total compliance (Eq. 4.2)

$$\mathbf{C}(\bar{c}, G_D) = \left(\frac{1}{3K(G_D)} + \frac{5}{2}\beta^e(G_D) N_0 \bar{c}^3\right)\mathbf{P}^{sp} + \left(\frac{1}{2G_D} + \frac{5-\nu}{2-\nu}\beta^e(G_D) N_0 \bar{c}^3\right)\mathbf{P}^d, \tag{4.31}$$

where Eq. (4.23) and Eq. (4.26) define $K(\bar{c})$ and $\beta^e(\bar{c})$ respectively. Finally, the instantaneous elasticity tensor is now:

$$\mathbf{E}(\bar{c}, G_D) = \mathbf{C}^{-1}(\bar{c}, G_D) = 3\hat{K}(\bar{c}, G_D)\mathbf{P}^{sp} + 2\hat{G}(\bar{c}, G_D)\mathbf{P}^{d} \tag{4.32}$$

and the damaged moduli (4.4), (4.5) are redefined as

$$\hat{K}(\bar{c}, G_D) = \frac{K(G_D)}{1+\kappa^e N_0 \bar{c}^3} \tag{4.33}$$

$$\hat{G}(\bar{c}, G_D) = \frac{G_D}{1+\gamma_t^e N_0 \bar{c}^3}\,. \tag{4.34}$$

Regarding the damage evolution, the damage surface now depends on G_D through $\sigma_{cr}(\bar{c}, G_D)$ as

$$F(\boldsymbol{\sigma}, \bar{c}, G_D) = \frac{\sigma_1}{\sigma_{cr}(\bar{c}, G_D)} - 1, \tag{4.35}$$

where

$$\sigma_{cr}(\bar{c}, G_D) \equiv \sqrt{\frac{\pi}{1-\nu}\frac{G_D \gamma}{\bar{c}}} \tag{4.36}$$

and (4.14) (4.15) become

$$\dot{\bar{c}} = \dot{c}_{\max}\left(1 - \frac{1}{1+\langle\frac{\sigma_1}{\sigma_{cr}(\bar{c}, G_D)} - 1\rangle}\right) \tag{4.37}$$

$$\dot{\bar{c}} = \dot{c}_{\max}\left(1 - \frac{1}{1+\langle\frac{\bar{E}(\bar{c}, G_D)\varepsilon_1(t)}{\sigma_{cr}(\bar{c}, G_D)} - 1\rangle}\right). \tag{4.38}$$

It is good to point out that $\bar{E}(\bar{c}), G_D, \sigma_{cr}(\bar{c})$ and $\bar{c}$ are numerically calculated (iteratively) concurrently during the same time step in the algorithm. Also, that the matrices are reduced to scalar values for the one-dimensional application that follows.

4.4 Finite Element Model Implementation

The basis for the structural implementation approach is the seminal work by H.L. Schreyer and Z. Chen, "One-Dimensional Softening with Localization", 1986 [43], where a unidimensional structure has two zones represented by two rod elements (FEM). One element accumulates damage (element 2) while the other one responds linear elastically (element 1). This is also a convenient framework to explore structural health monitoring schemes, where the damage is localized (in one element).

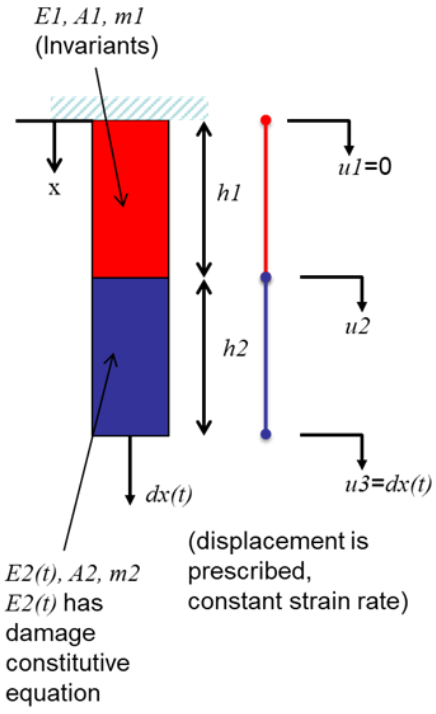

Figure 4.1 Structural Implementation Scheme.

The following section shows the derivation of the one-dimensional elements local matrices – mass (M) and stiffness (K); where a lump made assumption is put forward. Also, no damping (C) is considered for the very low strain rate phenomena analyzed. Later, the local matrices are assembled into global form to form the second-order ordinary differential equations of structural dynamics:

$$M\ddot{u} + Ku = p(t). \tag{4.39}$$

And lastly, the Newmark-β method is used to solve the ODE and implemented in MATLAB.

4.4.1 Local Matrices

Then, the local stiffness are:

$$K1 = \begin{bmatrix} k1 & -k1 \\ -k1 & k1 \end{bmatrix} \qquad K2 = \begin{bmatrix} k2(t) & -k2(t) \\ -k2(t) & k2(t) \end{bmatrix}, \tag{4.40a,b}$$

where

$$k1 = \frac{A1\ E1}{h1} \qquad k2\ (t) = \frac{A2\ E2(t)}{h2} \tag{4.41a,b}$$

and,

$$K = K1 + K2. \tag{4.42}$$

The local mass matrices are:

$$M1 = \begin{bmatrix} m1 & 0 \\ 0 & m1 \end{bmatrix} \qquad M2 = \begin{bmatrix} m2 & 0 \\ 0 & m2 \end{bmatrix}, \tag{4.43a,b}$$

where

$$m1 = \frac{\rho 1\ A1\ L1}{2} \qquad m2 = \frac{\rho 2\ A2\ L2}{2} \qquad (4.44a,b)$$

and,

$$M = M1 + M2. \qquad (4.45)$$

4.4.2 Global Matrices

Assembling the local matrices into global form to resolve (4.46)

$$M\ddot{u} + Ku = P(t)$$

$$\begin{bmatrix} m1 & 0 & 0 \\ 0 & m1+m2 & 0 \\ 0 & 0 & m2 \end{bmatrix} \begin{bmatrix} 0 \\ \ddot{u}2(t) \\ \ddot{u}3(t) \end{bmatrix} + \begin{bmatrix} k1 & -k1 & 0 \\ -k1 & k1+k2(t) & -k2(t) \\ 0 & -k2(t) & k2(t) \end{bmatrix} \begin{bmatrix} 0 \\ u2(t) \\ dx(t) \end{bmatrix} = \begin{bmatrix} r1(t) \\ 0 \\ p(t) \end{bmatrix} \qquad (4.47)$$

Taking into account the boundary conditions $\ddot{u}1(t) = u1(t)$=0 , then $\ddot{u}2(t)$ & $u2(t)$ are the unknowns and $\ddot{u}2(t)$ can be derived based on $u2(t)$ and dx(t):

$$\ddot{u}2(t) = u2(t)\frac{(k1+k2(t))}{(m1+m2)} + \frac{k2(t)\ dx(t)}{(m1+m2)}. \qquad (4.48)$$

4.4.3 Solving the ODE

Equation (4.47) can be solved numerically by using the Newmark-β integration method:

$$u_{n+1} = u_n + \dot{u}_n\ dt + \frac{dt^2}{2}\left((1-2\beta)\ddot{u}_n + 2\beta\ddot{u}_{n+1}\right) \qquad (4.49)$$

$$\dot{u}_{n+1}=\dot{u}_n + dt\ \Big((1-\gamma)\ \ddot{u}_n + \gamma\ \ddot{u}_{n+1}\Big). \tag{4.50}$$

Then, by using the previous step's stiffness value (E2); the solution to the displacement ($u2_{n+1}$) and velocity of node 2 ($\dot{u}2_{n+1}$) is found as:

$$u2_{n+1} = \frac{u2_n\big(1-a1(k1+k2_n)\big)+\dot{u}2_n dt+a1\ k2_n\ dx_n+a0\ k2_{n+1}\ dx_{n+1}}{1+a0(k1+k2_{n+1})} \tag{4.51}$$

$$\dot{u}2_{n+1}=\dot{u}2_n + a2\big(k2_n\ dx_n - u2_n(k1+k2_n)\big) +$$
$$+a3\ (k2_{n+1}\ dx_{n+1} - u2_{n+1}(k1+k2_{n+1}), \tag{4.52}$$

where $a0, a1, a2$ & $a3$ are defined for clarity below, where $M = m1 + m2$;

$$a0 = \frac{\beta dt^2}{M}\ ;\ a1 = \frac{(1-2\beta)dt^2}{2M}; a2 = \frac{(1-\gamma)dt}{M}; a3 = \frac{\gamma dt}{M} \tag{4.53a,b,c,d}$$

and $\gamma = \frac{1}{2}$, $\beta = \frac{1}{4}$ are Newmark parameters.

4.4.4 Model Assumptions for Main Correlation Effort

The model assumptions are intended to match the experimental conditions that will be used to validate the model. These are based on the seminal work by V.S Gapalaratnam and S.P. Shah, *Softening response of Plain Concrete in Direct Tension*, 1985. The cross-section of the model is the same as the test coupon on Ref. [44] and the total model's length (comprised of 2 elements) is the same of the gage length 3.23" used in the experiment.

The plain concrete material properties relevant to model variables were found to be inconsistent throughout the available literature [47]. Then, this work recovered critical model variables from available experimental results [44] and derived the rest of the necessary model variables. The monotonic tensile displacement on node 3 is considered for quasi-static phenomena as 1.0×10^{-6} m/s

Then, the model variables used are:

- Density [kg/m^3] $\rho = 2{,}300$
- Initial Matrix Shear Modulus [Pa] $G_0 = 1.57 \times 10^{10}$
- Poisson's ratio $\nu = 0.2$
- [Initial crack size [m] $\bar{c}_0 = 4.3 \times 10^{-5}$
- Crack number density [m^{-3}] $N_0 = 4.4 \times 10^{10}$
- Surface energy [J/m^2] $\gamma = 0.01$
- Time Step [s] dt=0.115

Chapter 5. Results

5.1 Introduction

This chapter presents the correlation of this modeling effort to experimental data. The main correlation effort (Section 5.3) is based on Ref. [44], Figure 6(a); curves 1 and 2, for the monotonic test on notched specimen with optical crack width monitored (MON) and monotonic test on unnotched specimen (MU) respectively. First, the correlation to the original DCA model with the assumptions from Section 4.4.4 is presented, that drove the need for an improvement. Then, the correlation of DCA_MSD model is shown, while also comparing the results to DCA behavior to discuss the differences in the physics of both models.

Additional correlation cases (2) are shown at the end of the chapter (Section 5.4) based on experimental data from Ref. [63] to demonstrate the applicability of the constitutive model and structural implementation scheme for different concrete mixes and coupon sizes.

It is good to point out that the results discussions in this work refer to displacement and not strain (which is more conventional) to make a direct and clear comparison to experimental data, which cite displacement and not strain. On that point, the final experimental displacement is 5.75×10^{-5} m, which is input in the model, and the prescribed loading condition is a linear ramp displacement at very low rate of 1.0×10^{-6} m/s.

As a clarification, the approach of having only one element of the two with the damage model is adequate for this analysis and the representation of the physics. The softening manifests in one element first, the one that reaches σ_{cr} first (Elm. 2, in this case), and then continues a focused softening process on that element. This in itself relieves/unloads the other element (Elm. 1), as node 2 becomes less reactive to the "pull" from the prescribed displacement (on node 3); which reduces the stress state on that element (unloads). This is not due to an increase in compliance, as is happening on Elm. 2, but to the reduction of strain caused by the elastic rebound of Elm.1, since E_1 remains constant.

Based on that reasoning, the bulk of the results that are shown is on Element 2 (Elm. 2) that features the damage material model. Element 1 results are linear elastic throughout by design.

5.2 DCA Results and Explanation of Behavior (Stress-Displacement)

From the stress-free state (**A**), the material is loaded in tension through prescribed displacement to 5.75×10^{-5} m (**E**) or 6.97×10^{-4} strain at 1.0×10^{-6} m/s displacement rate or 1.21×10^{-5} strain rate. The total event takes 57.5 seconds in the modeling and is considered quasi-static. The bold letters in this paragraph serve as markers for the plots below.

The DCA Model shows adequate correlation up to the peak stress value and start of the softening phase (**A-B-C'-D'**), but the model diverges for the rest of the softening phase (**D'-E'**). Consequently, the model captures the most important physics from a structural analysis concern but does not fully characterize the response. The model still

does not feature enough compliance during the softening phase, or in other words, the stiffness degradation due to damage is not enough to reflect the experimental response.

The stress evolution from **A** to **B** marks the linear response of the material. In this area, the crack size remains constant and equal to the initial value. In other words, there is no crack growth for this period and DCA calculates the response using a slightly damaged modulus that takes into account the initial crack size $\bar{c}_0 = 4.3\text{x}10^{-5}$.

Point **B** marks the instant when the stress state first reaches the damage surface and the beginning of crack growth. The damage surface progressively contracts with increased strain. The damage and rate of crack growth are not enough at this time to revert the stress rate and the response remains strain hardening until point **C** is reached. This is primarily due to the small size of the cracks.

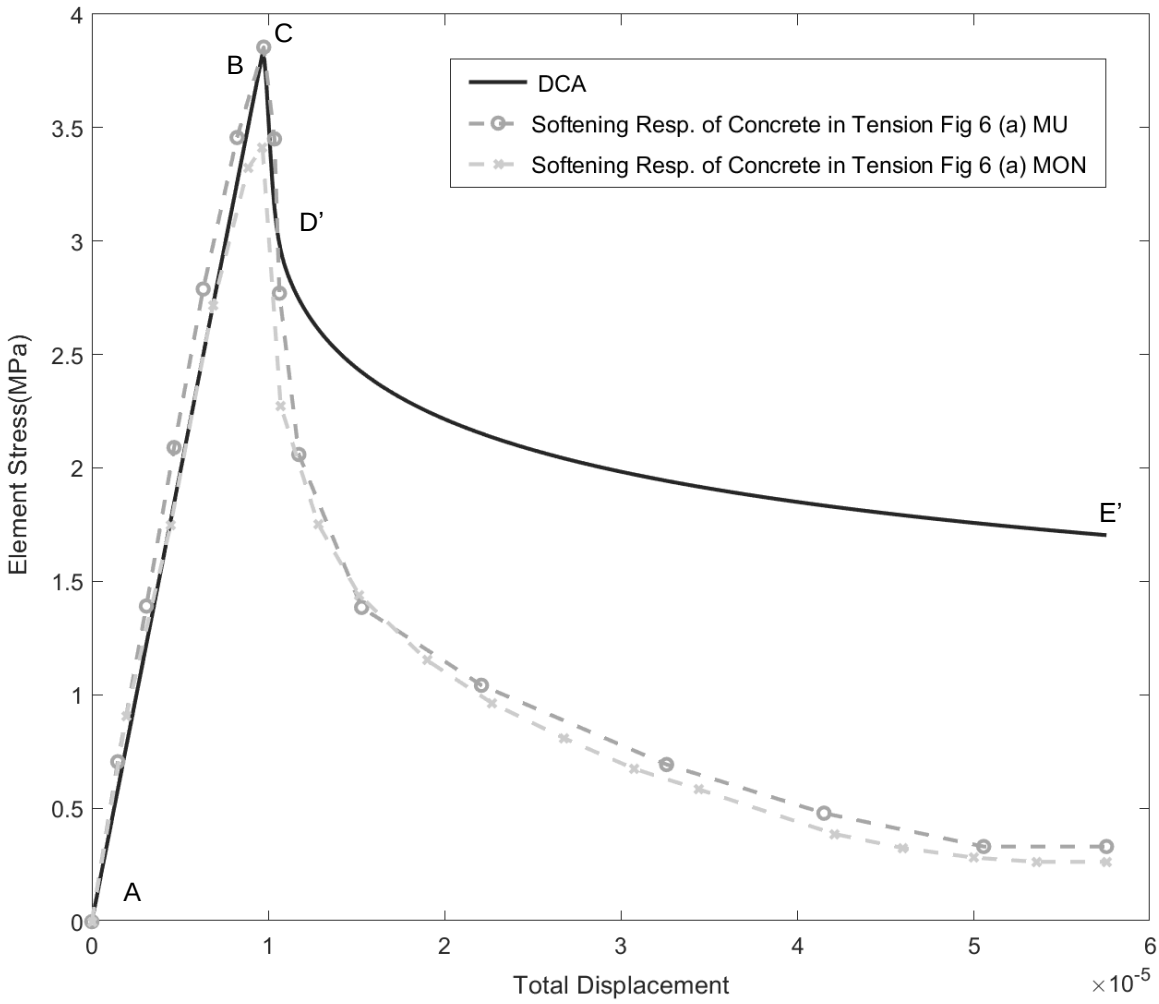

Figure 5.1 DCA Correlation to Experimental Data [44] and Comparison.

After this peak, the strain rate due to crack growth reaches and surpasses the total strain rate $\dot{\varepsilon}$ giving way to a rapid softening period (**C-D'**). This segment still shows good agreement with experimental data in Ref. [44].

Beyond point **D'**, the cracks continue to grow, but at a slower rate. During this segment (**D'-E'**), the increased compliance reduces the stress state in the material, and with that, the rate of crack growth. It can also be seen in the plot below, that although the material has reduced stiffness due to damage (**D'-E'**), the damage accumulation is not

enough to match the experimental data. In other words, the residual instantaneous elastic modulus is too high, and the material is still too reactive (still) to the strain.

5.3 DCA_MSD Results

5.3.1 Stress-Displacement

The DCA_MSD model also correlates well through the linear elastic phase (**A-B**), peak stress (**C**) and initiation of the softening phase (**C-D'**). Both models respond similarly up to a displacement of ~0.0103 mm (**D'**).

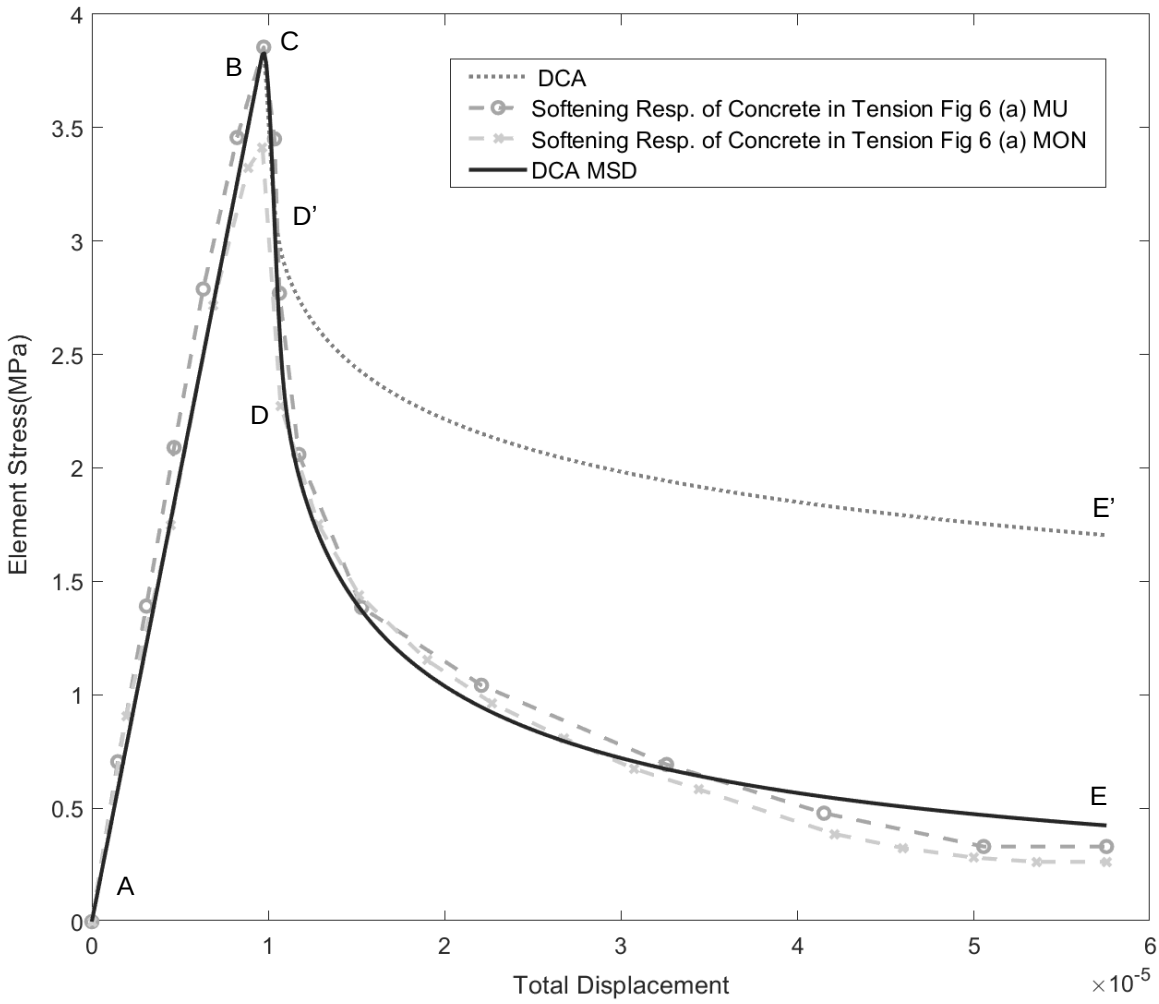

Figure 5.2 DCA & DCA_MSD Correlation to Experimental Data [44] and Comparison.

After this elongation, the physics of the softening phase is much different for DCA_MSD. The coupled interaction between the reduction in Shear Modulus of the matrix $G(\bar{c})$ and crack growth $\dot{\bar{c}}$ becomes relevant. It is noticeable that the "rapid softening" phase where there is a large increase in compliance right after the peak stress is much longer (**C-D**), which ultimately allows for a correlation error reduction of 387%, from 1.37 MPa to 0.09 MPa at total elongation.

This is a significant improvement to the model and signifies new physics.

5.3.2 Crack Growth

Crack growth and final crack size are affected by the new physics. Damage is now coupled (compounded) and the material does not necessitate “as large” crack size to accrue the same damage.

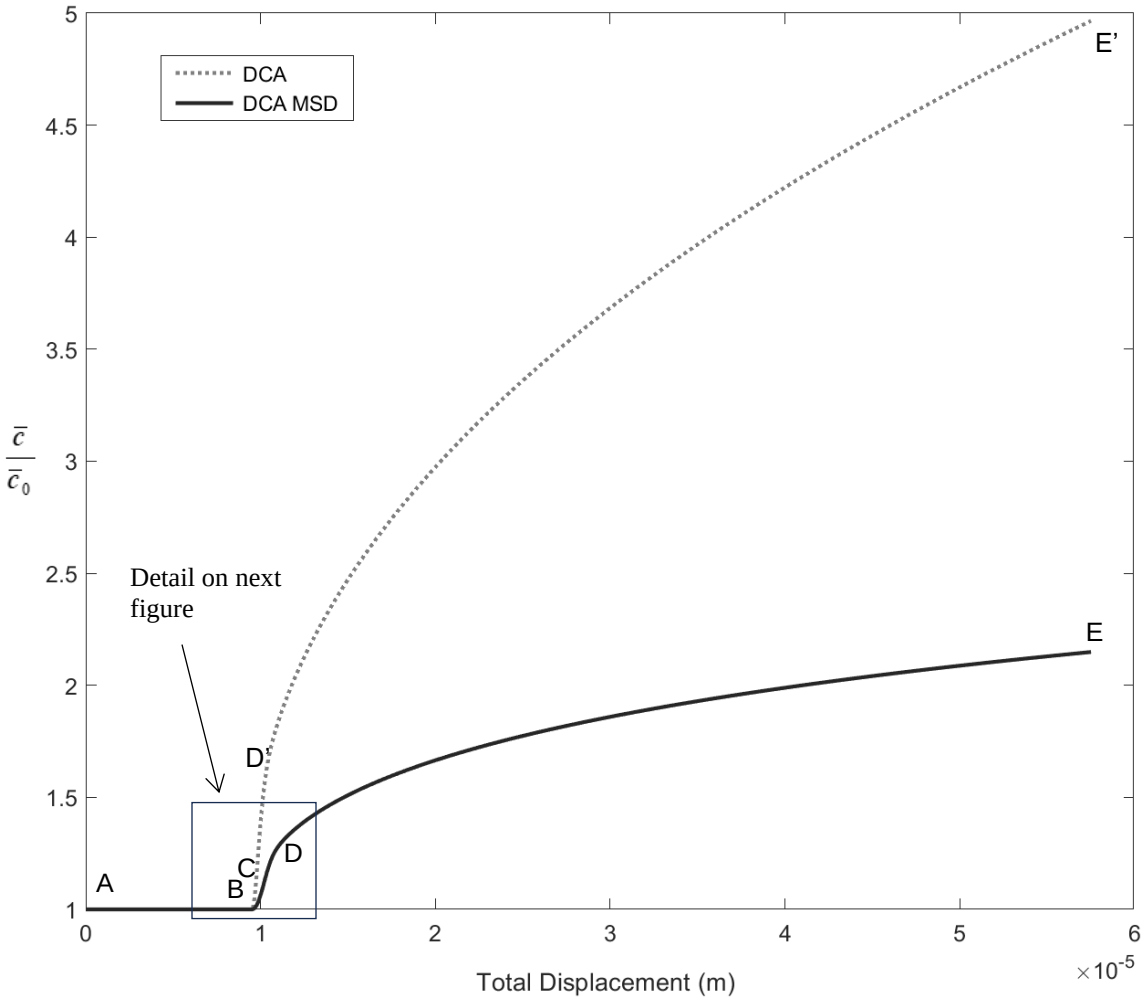

Figure 5.3 DCA & DCA_MSD Crack Growth.

Crack growth also slows down in the improved model based on the further damaged E and G that reduces the stress around the crack. A different way to see this phenomenon

is that the total damage is more sensitive to crack growth. Where in DCA a crack reaches ~5x the original size at the end of the model run (**D'**), DCA_MSD features 2.15x the original crack size, a reduction of ~57%, and with significantly increased compliance (**D**).

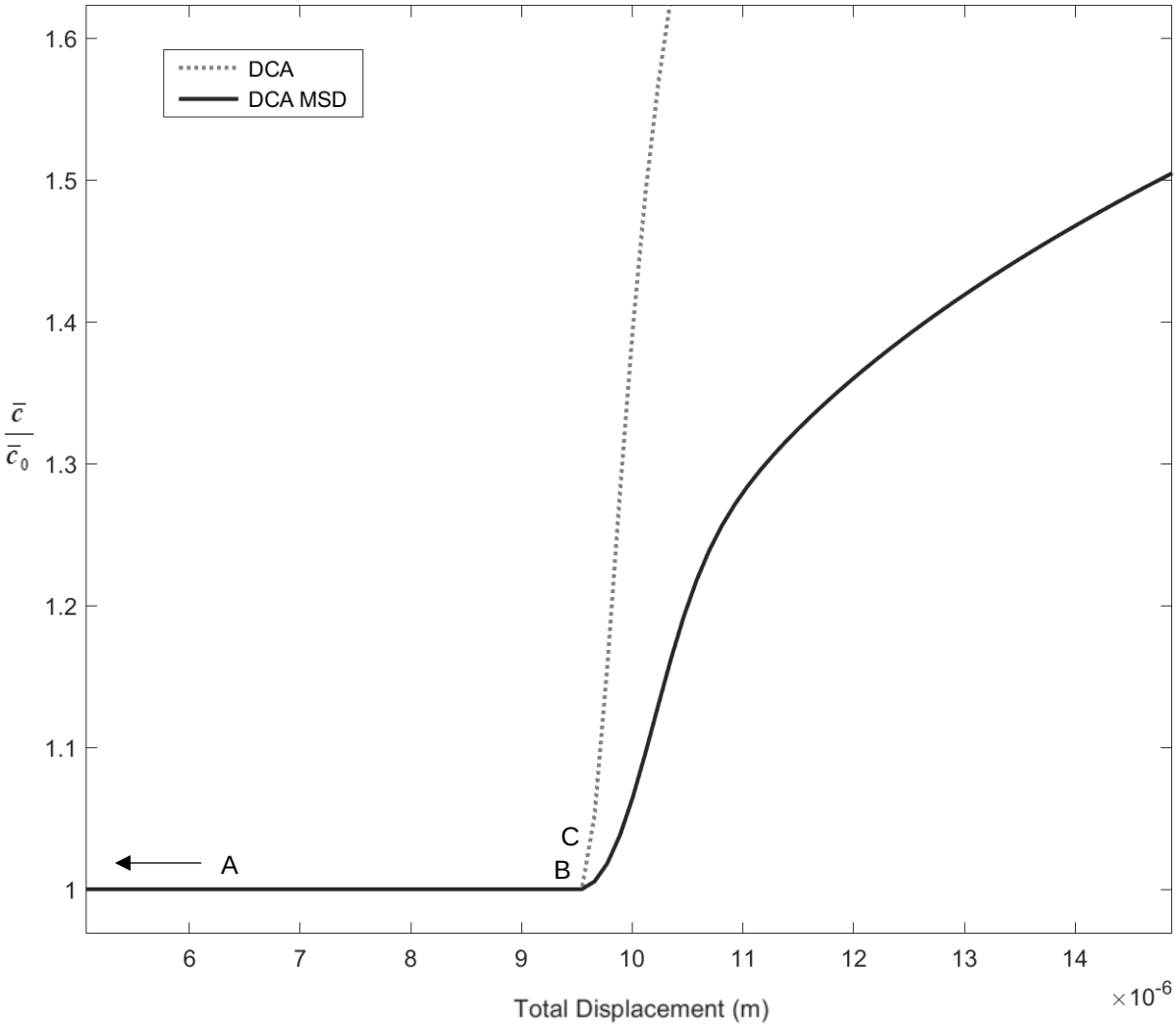

Figure 5.4 DCA & DCA_MSD Crack Growth Initiation.

The increased compliance of DCA_MSD is also seen at the start of crack growth too at ~0.0095 mm (**B**); where the crack growth requires more displacement to occur (softer curve).

5.3.3 Instantaneous Elasticity Modulus

Degradation of E starts with crack growth at ~0.0095 mm. Both models respond similarly up to a displacement of ~0.01 mm. The degradation of the stiffness is now compounded with the Shear Modulus G damage which accelerates the total damage and concludes in a further decreased Elasticity Modulus.

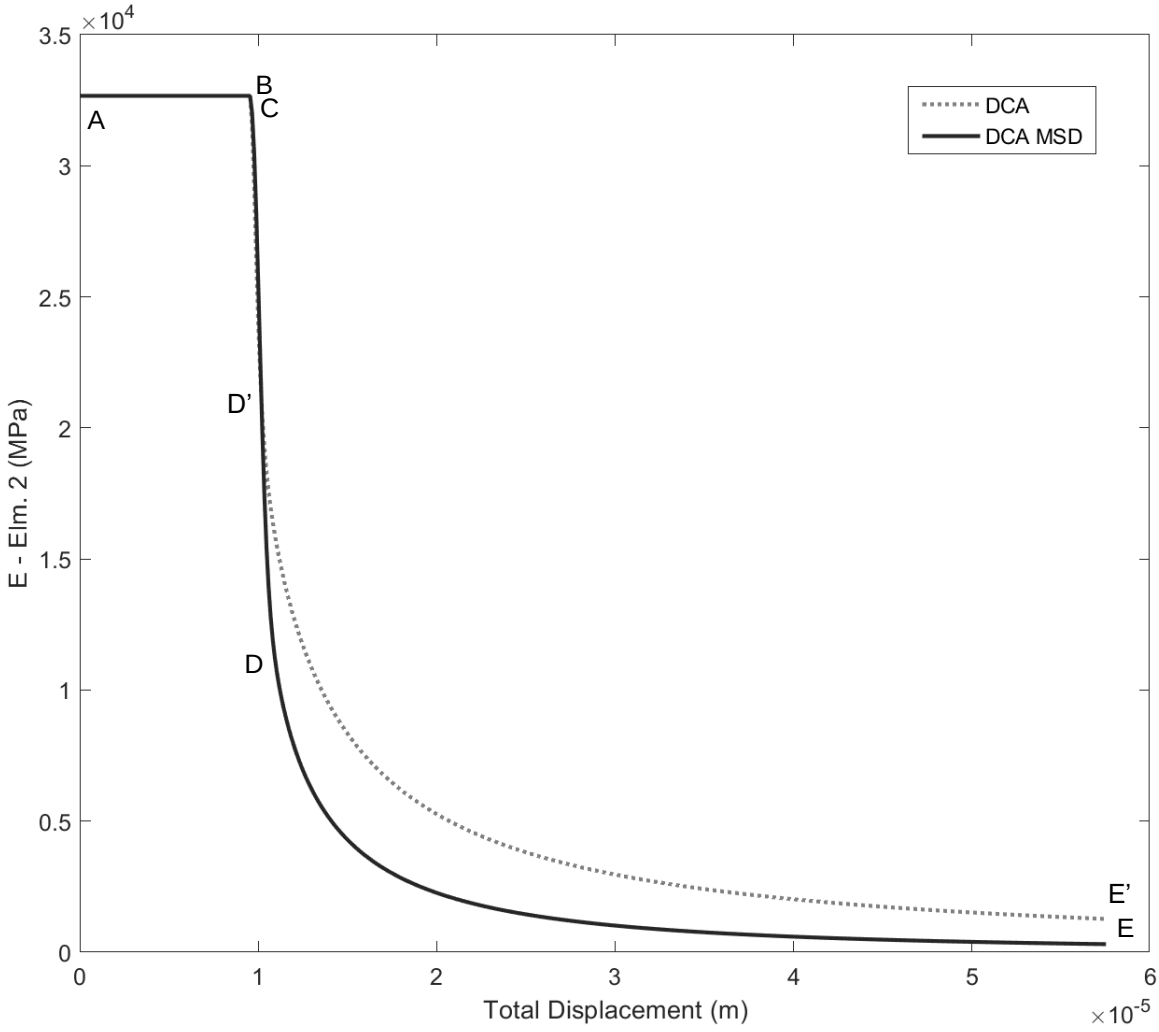

Figure 5.5 DCA & DCA_MSD Inst. Elasticity Modulus.

The final reduction on E is ~76% compared with DCA and ~99% compared to the linear elastic phase (**A-B**).

5.3.4 Nodes Displacement (Elements' Elongation)

The plots below denote the elongation of both elements. The bifurcation shown represents when the damage accumulation is sufficient to diverge enough from the linear elastic response, right around peak stress (**C**).

Elm. 2 (Node 2-Node 3) contains the damage function and shows significant elongation, 26 times that of Elm. 1 (Node 2) under the prescribed displacement (**E**). Furthermore, the plots below show the rebound displacement of Node 2 (displacement changes direction) due to unloading from strain softening being experienced in Elm. 2 (**C-D-E** & **C-D'-E**').

Increased compliance of Elm. 2 on DCA_MSD releases node 2 (**C-D**) longer than the original DCA model (**C-D'**) which results in Elm. 1 reaching a shorter elongation (larger rebound) and Elm#2 compensating with larger elongation, since the model is displacement controlled (total elongation is prescribed).

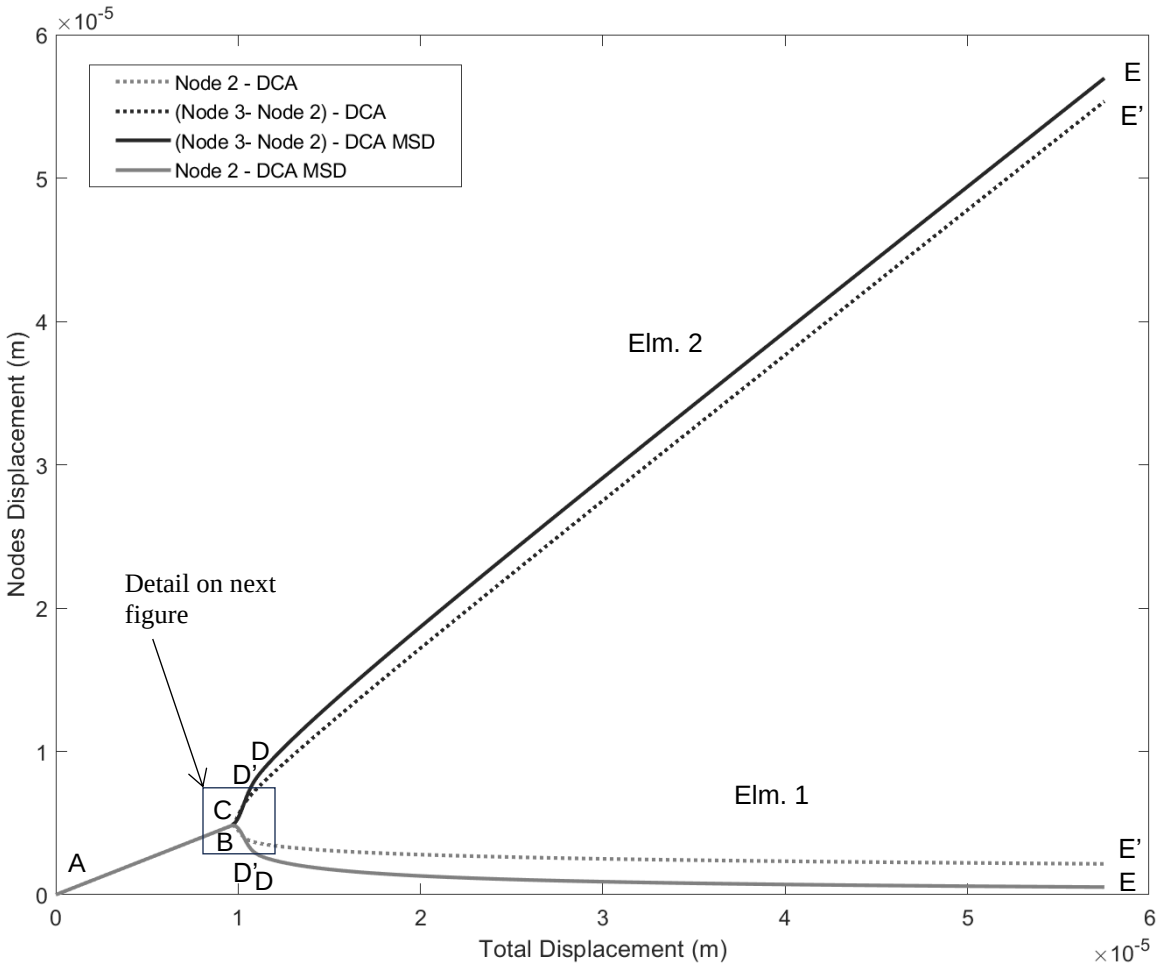

Figure 5.6 DCA & DCA_MSD Nodes Displacement.

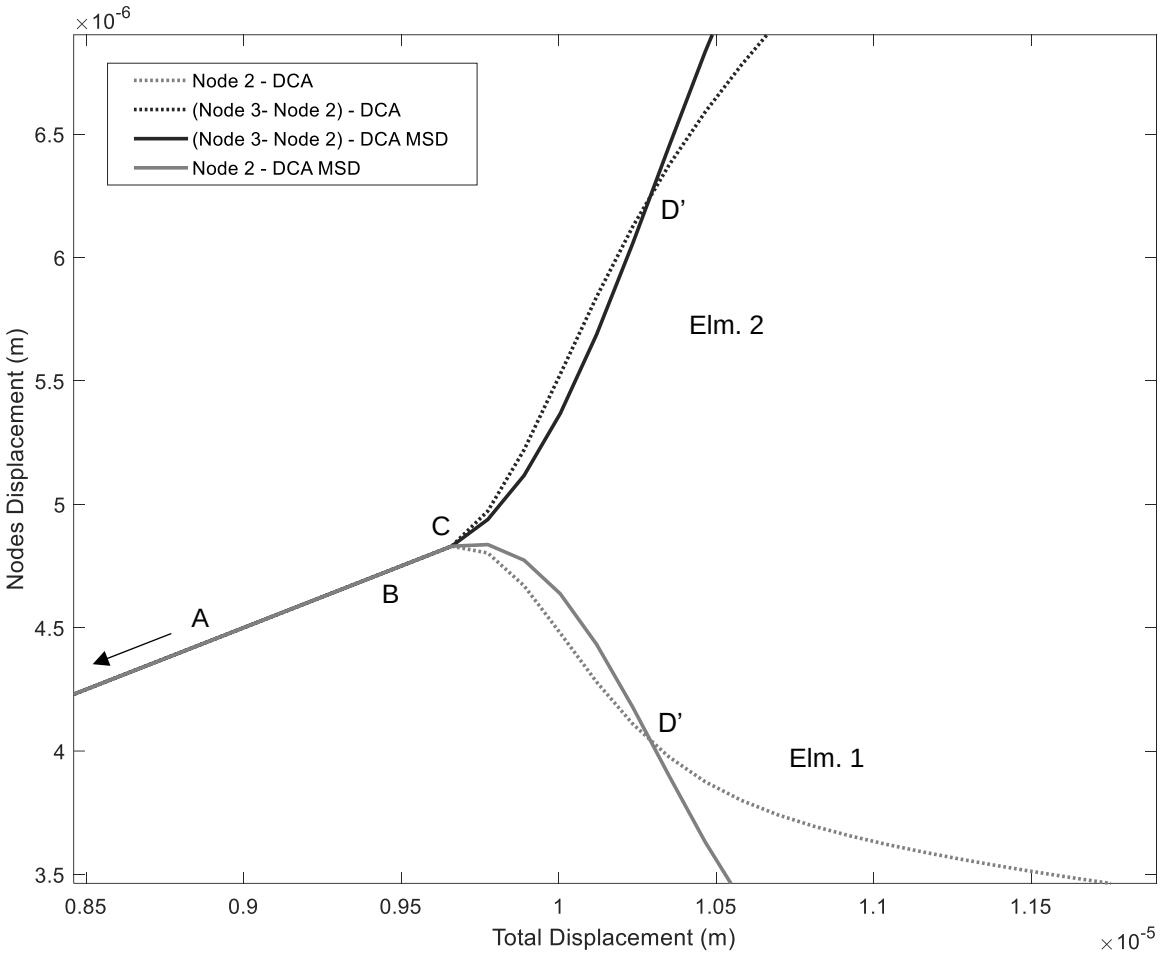

Figure 5.7 DCA & DCA_MSD Nodes Displacement.

Increased compliance from the start of damage accrual causes slower node displacement initially for DCA_MSD (**C**). Nevertheless, total damage on DCA_MSD then accelerates and overtakes DCA at ~0.0103 mm total displacement (**D'**); where both models start to significantly diverge.

5.3.5 Node 2 Acceleration

As discussed before, DCA_MSD total damage then overtakes DCA at ~0.0103 mm total displacement (**D'**). The increased compliance of Elm. 2 releases node 2 for longer (**C-**

D') than the original DCA model (**C-D'**). Consequently, Node 2 deceleration phase for DCA_MSD is also longer (**C-D**). This causes the final acceleration (**E**) to be also lower (less reactive) and reduces ~76% from DCA values (**E'**).

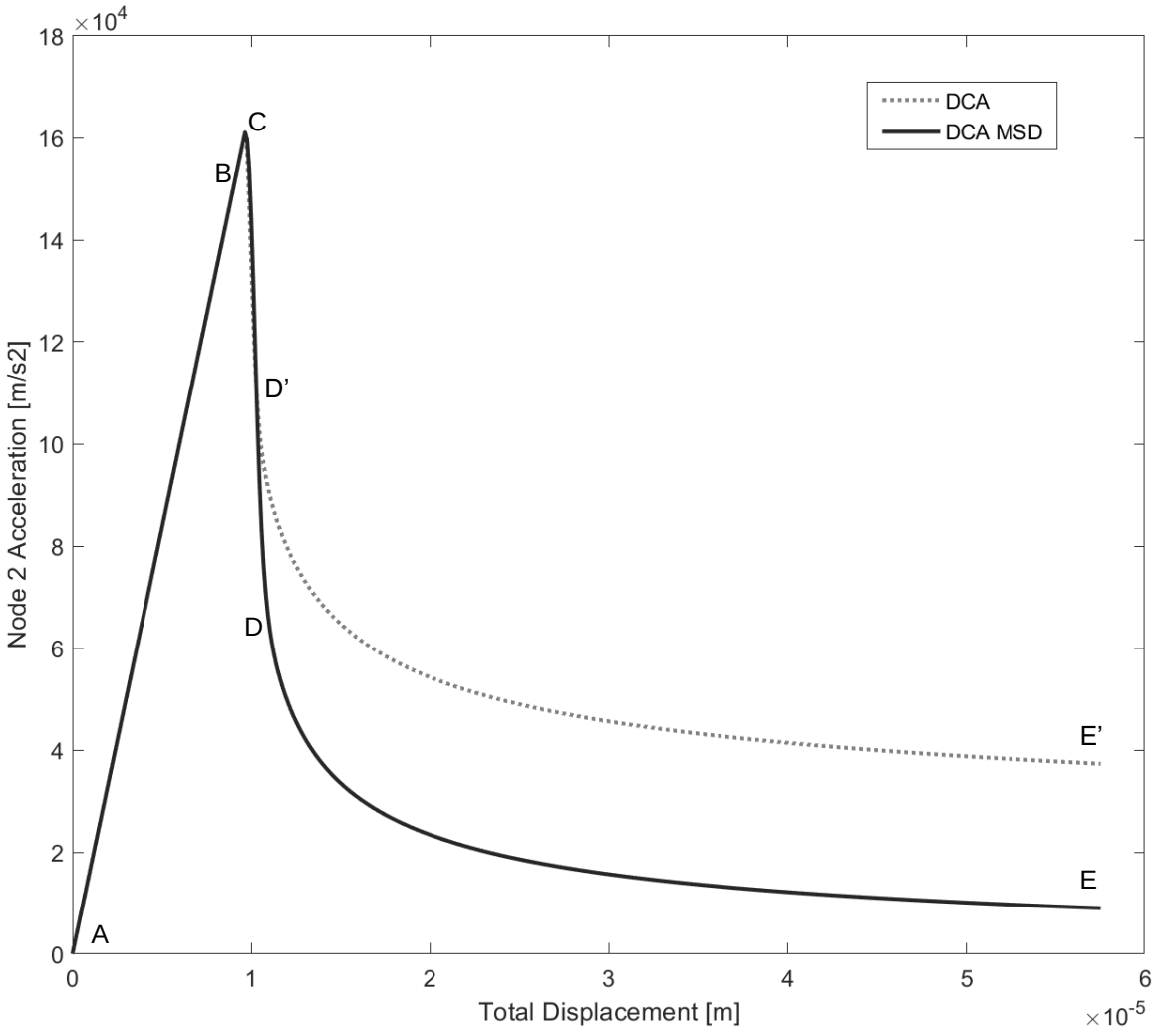

Figure 5.8 DCA & DCA_MSD Node 2 Acceleration.

5.3.6 Matrix Shear Modulus Degradation

This plot shows the Shear Modulus of the matrix damage accumulation progression, that is not present in the original DCA model (where it remains constant). The

matrix Shear remains constant through the linear elastic response phase (and same value as DCA, **A**-**B**). The degradation of G starts with the initiation of crack growth at ~0.0095 mm, the same time as E.

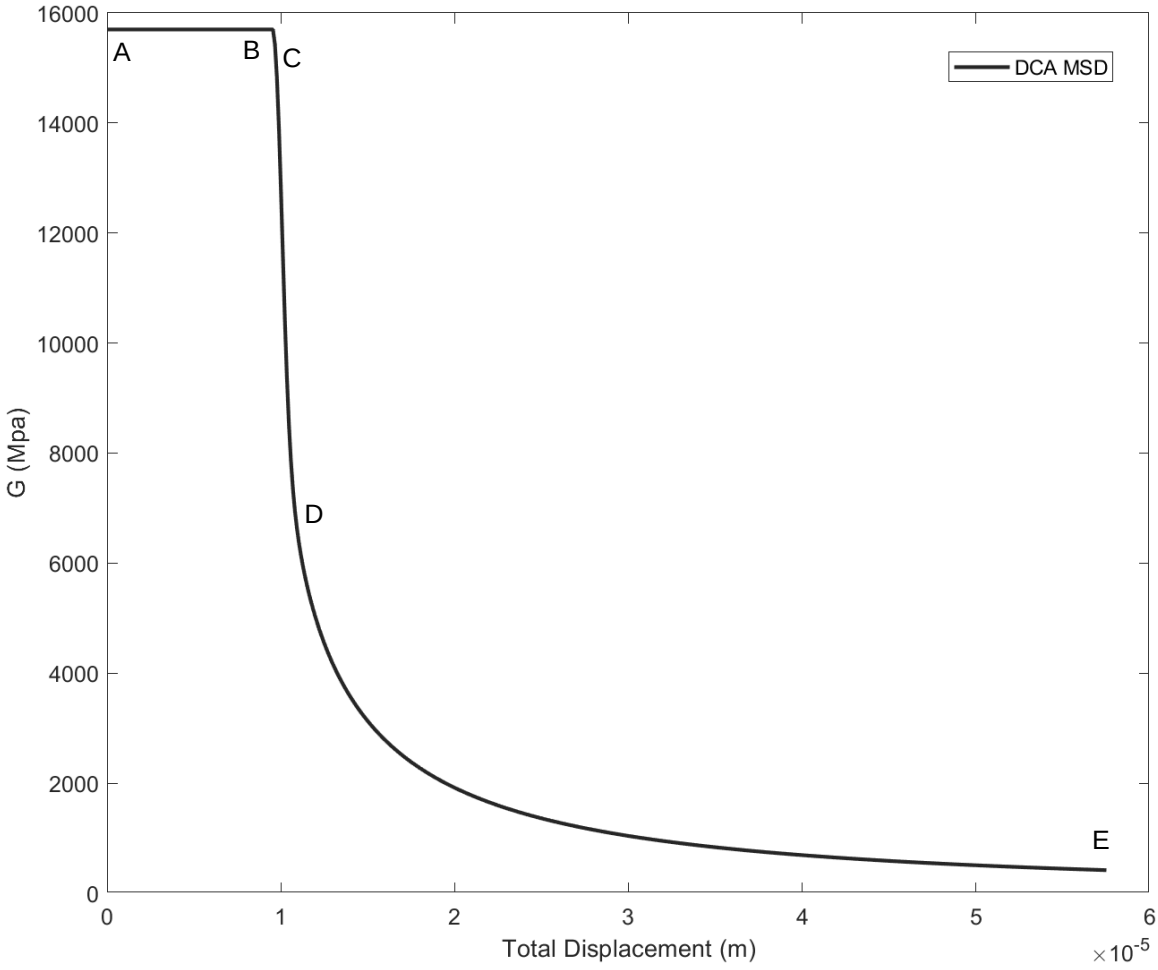

Figure 5.9 DCA & DCA_MSD Matrix Shear Modulus.

By the end of the deformation (**E**), the Shear Modulus of Elm. 2 is degraded ~97% in comparison to the initial value. This effect is the most significant feature of the proposed model; and causes the most relevant impact on the improved correlation to experimental data.

5.3.7 Exponential Factor Study

It is good to point out that the new damage accrual on Matrix Shear arose from the discovery that tying G degradation to E was effective and physically relevant. Although that approach provided good correlation with experimental data, it also featured inconsistent physics for crack growth behavior; and was not implementable in the implicit algorithm. Considering the shear degradation solely dependent on crack growth solved these shortcomings, allowed for concurrent calculations in the implicit algorithm routine (same time step) and was consequently selected as the approach going forward. Furthermore, an exponential relation was selected for simplicity and efficacy.

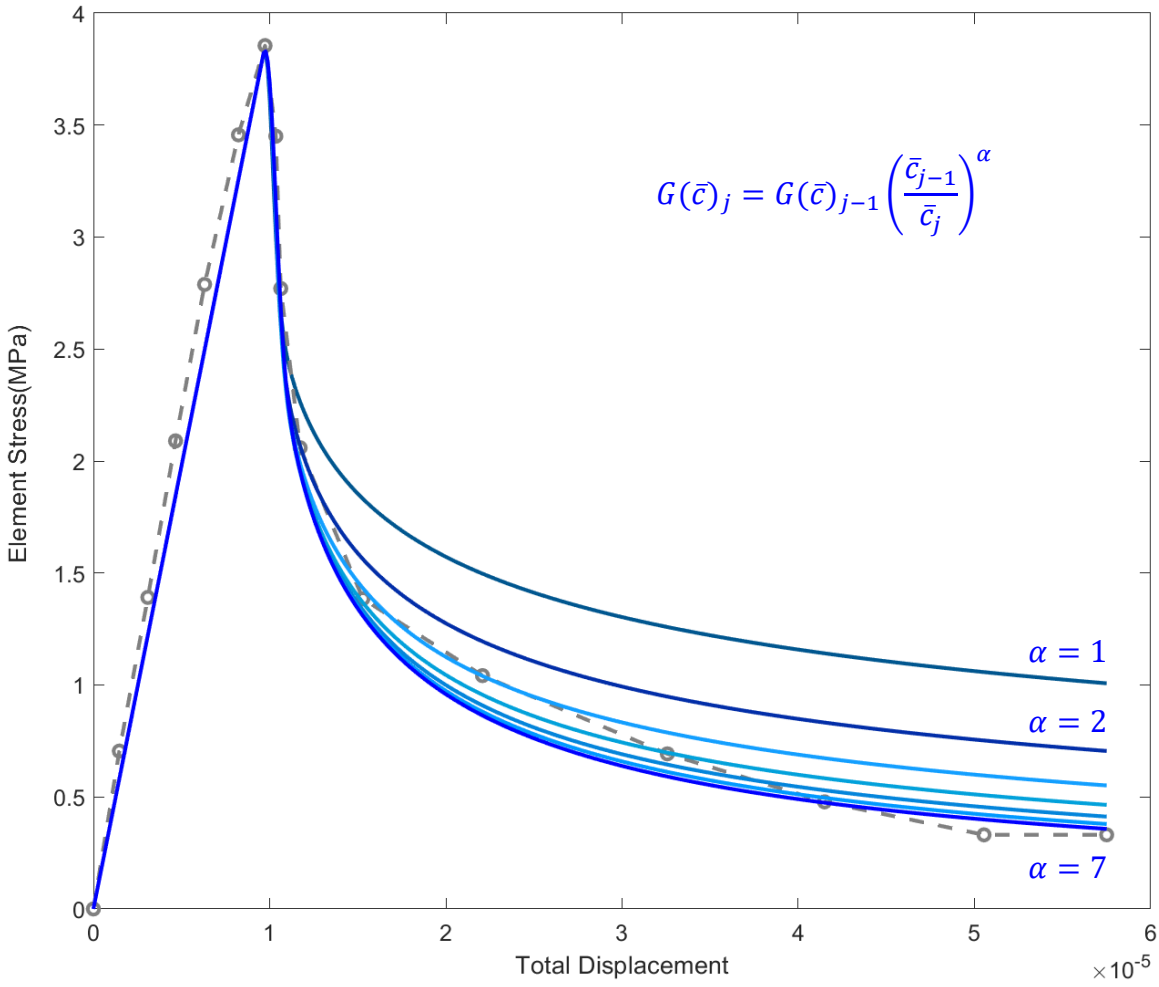

Figure 5.10 Exponential Factor Study.

Several values for the exponential term were considered in sensitivity studies. The exponential term based on the rate of the instantaneous crack compared to the initial crack was ultimately selected since it allows for increased influence at higher strain; and showed good correlation to experimental results [44].

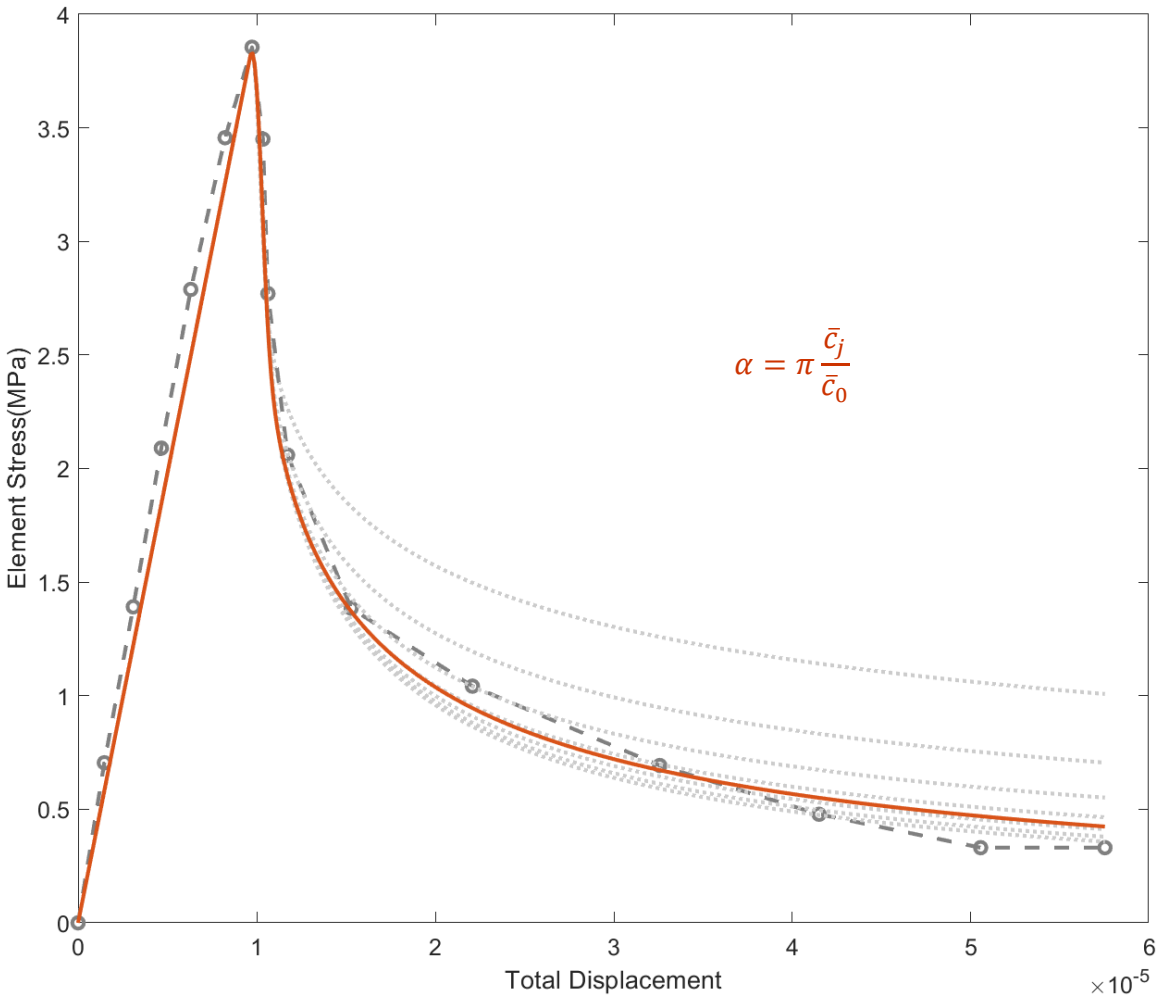

Figure 5.11 Selected Exponential Factor.

5.4 Additional Correlation Cases

In order to demonstrate the robustness and applicability of the new constitutive model DCA_MSD and structural implementation scheme, an additional correlation effort to experimental data was conducted. The experimental data for the two additional cases evaluated in this section are based on Hordijk, 1991 [63].

5.4.1 Specimen Type A

This section evaluates the correlation to Hordijk, 1991, Specimen Type A, from figure 5.6(a) in reference [63]. The coupon size for this case is 250×60×50 mm^3 with a symmetric notch of 5 mm and a gage length of 35 mm. The surface area used to calculate the stress is 50×50 mm^2. The test specimen was constructed from lightweight concrete (LC) as per reference [63] Appendix A. The tests were displacement controlled, uniaxial monotonic tensile and cyclic. The final displacement was 0.1 mm.

The model variables used for this case are:

- Density [kg/m^3] $\rho = 1{,}829$
- Initial Matrix Shear Modulus [Pa] $G_0 = 1.2\text{x}10^{10}$
- Poisson's ratio $\nu = 0.2$
- [Initial crack size [m] $\bar{c}_0 = 4.8\text{x}10^{-5}$
- Crack number density [m^{-3}] $N_0 = 1.2\text{x}10^{11}$
- Surface energy [J/m^2] $\gamma = 0.01$
- Time Step [s] dt = 0.2

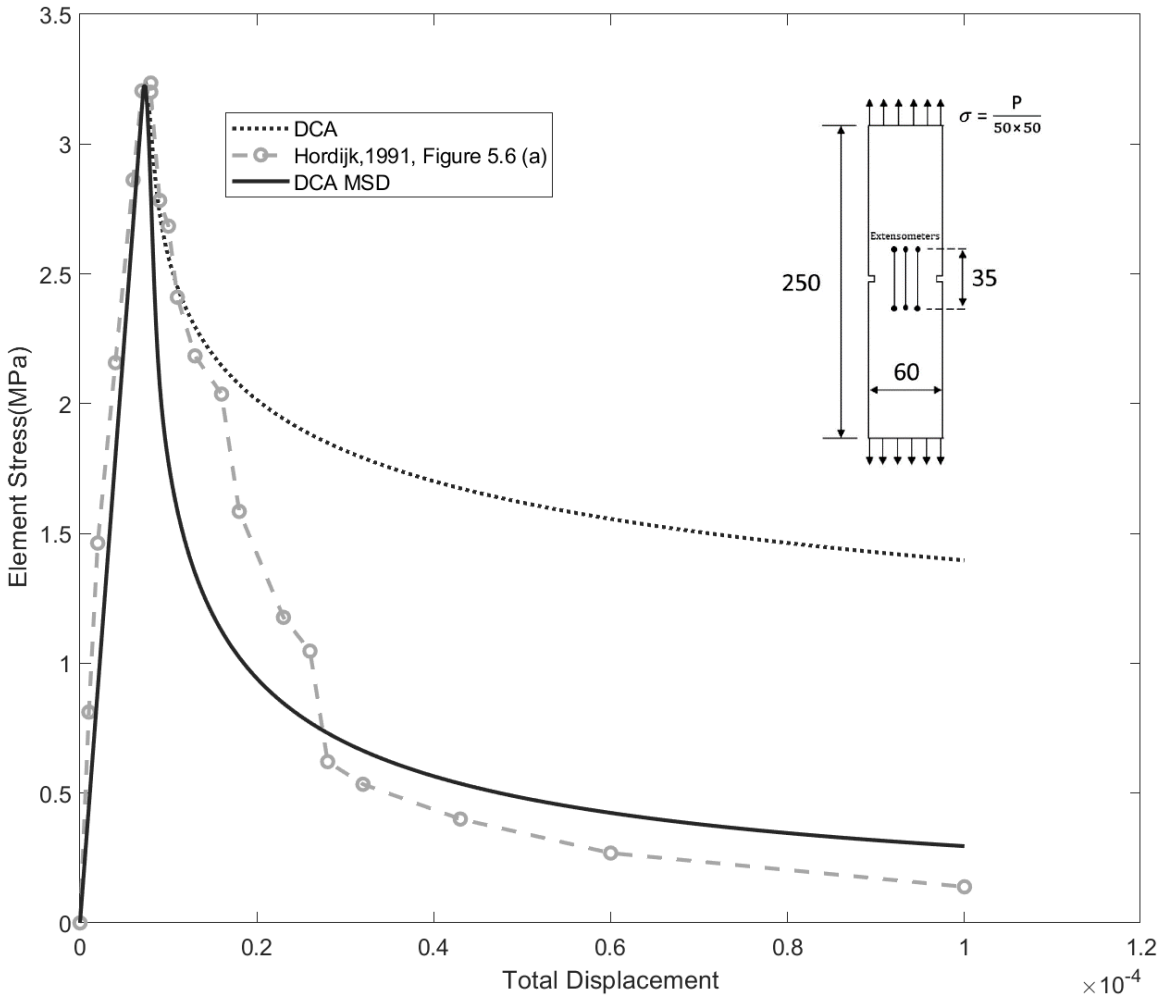

Figure 5.12 DCA & DCA_MSD Correlation to Experimental Data [63] and Comparison– Specimen Type A.

As with the main correlation effort in Section 5.3, DCA shows adequate correlation for the linear elastic portion, peak stress and start of softening phase. The DCA_MSD model features good correlation overall, and a marked improvement from DCA results, as previously seen in the main correlation effort from Section 3.5. Although it is not as well correlated as before (with Gapalaratnam & Shah data), especially during the accelerated softening right after peak stress, Hordjik noted that the "descending branch displayed irregularities", which were most notable on the LC samples that are being considered in

this effort. The irregularities are assumed to be due to testing difficulties, rotation of the specimens and asymmetrical crack growth. “Cleaner” experimental data may feature improved correlation.

5.4.2 Specimen Type D

This section evaluates the correlation to Hordijk, 1991, Specimen Type D, from figure 5.6(d) in reference [63]. The coupon size for this case is 250×50×40 mm^3 with a symmetric notch of 5 mm and a gage length of 35 mm. The surface area used to calculate the stress is 40×40 mm^2. The test specimen was constructed from lightweight concrete (LC) as per reference [63] Appendix A. The tests were displacement controlled, uniaxial monotonic tensile and cyclic. The final displacement was 0.1 mm.

Then, the model variables used for this case are:

- Density [kg/m^3] $\rho = 1{,}829$
- Initial Matrix Shear Modulus [Pa] $G_0 = 1.48\text{x}10^{10}$
- Poisson’s ratio $\nu = 0.2$
- [Initial crack size [m] $\bar{c}_0 = 4.5\text{x}10^{-5}$
- Crack number density [m^{-3}] $N_0 = 2.15\text{x}10^{11}$
- Surface energy [J/m^2] $\gamma = 0.01$
- Time Step [s] dt = 0.2

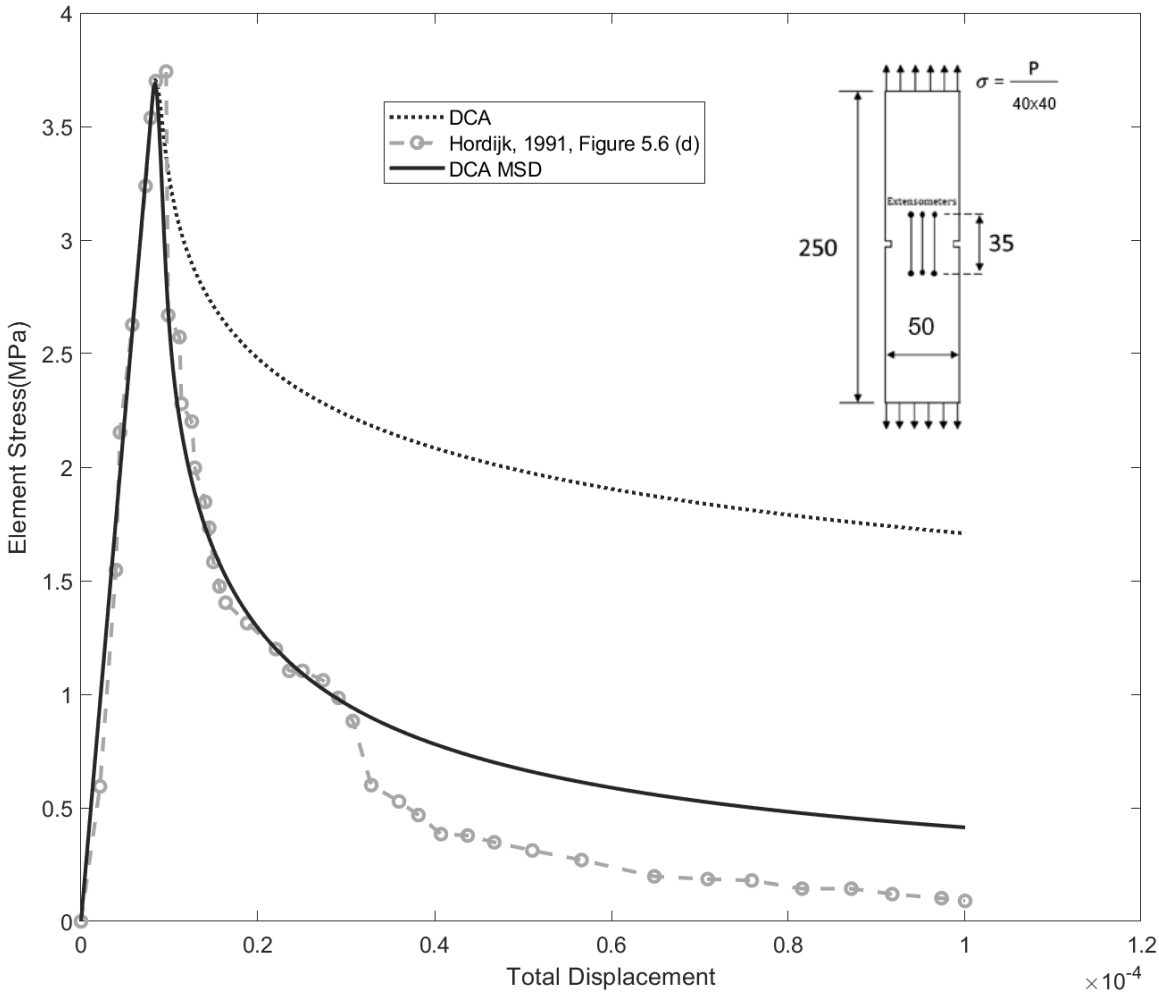

Figure 5.13 DCA & DCA_MSD Correlation to Experimental Data [63] and Comparison–Specimen Type D.

As with the main correlation effort in Section 5.3, DCA shows adequate correlation for the linear elastic portion, peak stress and start of softening phase. The DCA_MSD model features good correlation overall, especially for the accelerated softening phase, right after the peak stress, and a marked improvement from DCA results. Although it is not as well correlated as before (with Gapalaratnam & Shah data) for the final phase of the softening, Hordjik noted that the "descending branch displayed irregularities", which were most notable on the LC samples that are being considered in this effort. The irregularities

are assumed to be due to testing difficulties, rotation of the specimens and asymmetrical crack growth. “Cleaner” experimental data may feature improved correlation.

Chapter 6. Conclusions and Future Work

6.1. Conclusions

Through this research, a constitutive model named DCA_MSD was developed. This model improves the original DCA model from Zuo *et al.* 2006 through a coupled damage assumption that incorporates damage in the Matrix Shear Modulus, which is considered directly dependent on crack growth. This allowed for the new damaged Matrix Shear Modulus to be incorporated into an implicit algorithm and calculated concurrently with the average instantaneous crack size, Elasticity Modulus and Tensile Strength of the Material. The predicted structural responses match well with experimental data. Key findings are summarized below:

- A new brittle damage constitutive model was developed.

This was accomplished by the incorporation of the new coupled damage assumption. An exponential relationship for the new damage variable was deemed to provide adequate physical representation of the damage evolution and was numerically efficient.

- The constitutive model was implemented into a structure.

The DCA model and the new material model DCA_MSD were reduced to 1-D form and subsequently implemented into a structure in order to validate the response with experimental data. This was done by developing a finite element model (FEM) in MATLAB. The FEM represented a rod and was composed of 2 elements (and 3 nodes),

one that contained the damage material model and the other assumed linear elastic characteristics. That approach was reflected in the local stiffness and mass matrices, which were then converted into global matrices to form the equation of motion. The equation of motion was later resolved through a numerical scheme based on the Newmark-β integration method.

- Structural analysis and model validation with experimental data were conducted.

The damage model variables were derived for plain concrete at very low strain rate and incorporated into the models. Boundary conditions for the FEM were made to match the experimental results that would be used for correlation [44] [63]. A quasi-static ramped monotonic prescribed displacement was applied at one end of the rod (node 3), while the other end was fixed (node 1).

The two finite element models, one containing DCA and another one with DCA_MSD were run on MATLAB for the boundary conditions selected [44] [63].

For the main correlation effort (Section 5.3) the model containing the original DCA scheme featured adequate correlation for the most significant structural analysis characteristics of the response, up until right after peak stress and initiation of the softening phase. Nevertheless, DCA did not render good correlation throughout the full softening phase, rapidly diverging after the initiation of softening and retaining significant residual stiffness compared to experimental results.

On the other hand, the improved model DCA_MSD captured the full strain-softening phase. DCA_MSD model features good correlation to experimental data throughout the material response at quasi-static load conditions.

The proposed improvement, incorporating damage based on crack growth in the Matrix Shear Modulus (DCA_MSD) and also account for coupled damage, showed to further increase material compliance during the softening phase of the response; which was an issue to improve on DCA. This is the first time that good correlation was demonstrated for the full loading cycle for a model derived from DCA at very low strain rate.

For the main correlation effort (Section 5.3) the stress-displacement correlation error was reduced ~387%, from 1.37 MPa to 0.09 at the end of the softening phase. The compliance increase was driven by the degradation of G by 97% and E by 99% compared to initial (linear elastic phase) values. The physics that drive crack growth is significantly changed, showing growth slowdown and a final average crack size that is significantly smaller, a ~57% reduction from DCA.

An additional correlation study in Section 5.4 showed similar results and conclusions for different concrete mixture and sample sizes [63]; demonstrating the applicability of the new constitutive model and structural implementation scheme.

- The design of structural health monitoring (SHM) scheme for brittle material structures was benefited by this research.

As discussed previously, elastic wave speeds in brittle materials are sensitive to changes in the mean size of distributed microcracks [42]. Then, measuring the wave speed in a material provides a practical means to determine the health state of a structural component made of such material.

The newly developed constitutive material model, as implemented and validated in the structural component herein, provides the required relationship between mean crack size, damage state and elastic wave speed needed to design a SHM scheme. This was first

achieved in this work by capturing the full response of the material, including elastic phase, maximum stress and strain softening phase up to failure, and featuring good correlation to experimental data throughout.

6.2. Recommendations for Future Research

Several steps could be taken to further the presented work. Next steps would include the construction of a comprehensive database of candidate extraterrestrial concrete materials to be used in additive manufacturing under Martian or Lunar environmental conditions. As discussed in Chapter 1, a more definite understanding of raw *in-situ* materials and feasible processes to synthesize concrete is needed. The database can then be verified by Martian and Lunar samples from future missions. In the meantime, the utilization of proxy materials and processes, such as soil simulants and in-orbit 3D printing will help further verify the model.

On that point, a more comprehensive modeling effort for different concrete mixes and mortars under other loading conditions, stress states and sample sizes can further validate the modeling approach and constitutive model.

Ultimately, the harsh and remote locations where the habitats and infrastructure will reside makes structure health monitoring an imperative for the safety crew that will depend on them. Visual inspection may be too risky or even impossible. Also, it is being considered that robotic and automated habitat construction will precede colonization, so remote monitoring (from Earth) of structural integrity of habitats is desired. To this end, it has been demonstrated in [42] that elastic wave speeds of a brittle material prove sensitive to changes in the mean size of distributed microcracks in the material. In other words, this

framework provides a practical means to deduce the size of cracks, or damage state, of the material by measuring its wave speeds.

Then, by further collecting physical insights from the simulation results of the proposed constitutive model, while assuming the availability of a comprehensive database of *in-situ* concretes (with known baseline wave speeds measured in intact material) and sophisticated signal processing techniques, a new structural health monitoring (SHM) scheme can be put forward.

References

[1] Muhammad Nazrif Zamani *et al.* (2022), *Preliminary study on radiation shielding properties of sulfur concrete on Mars,* IOP Conf. Series: Materials Science and Engineering, International Nuclear Science, Technology and Engineering Conference 2022

[2] Jiawen Liu *et al.* (2021), *In-situ resources for infrastructure construction on Mars: A review,* International Journal of Transportation Science and Technology

[3] Yushen Wang *et al.* (2022), *In-situ utilization of regolith resource and future exploration of additive manufacturing for lunar/martian habitats: A review,* Applied Clay Science

[4] Nicos Kalapodisa *et al.* (2020), *A review towards the design of extraterrestrial structures: From regolith to human outposts,* Acta Astronautica

[5] Benjamin Kading, Jeremy Straub (2014), *Utilizing in-situ resources and 3Dprinting structures for a manned Mars mission,* Acta Astronautica

[6] Yonathan Reches (2019), *Concrete on Mars: Options, challenges, and solutions for binder-based construction on the Red Planet*, Cement and Concrete Composites

[7] Duke *et al.* (2003), *Lunar resource utilization: Implications for commerce and exploration,* Advances in Space Research

[8] Ziyuan, O., Fugen, X. (2012), *Mars and its environment.* Spacecraft Environ. Eng. 29 (06), 591–601.

[9] Williams, D.R. (2004), *Mars Fact Sheet.*

[10] Duri G. *et al.* (2022) *The Potential for Lunar and Martian Regolith Simulants to Sustain Plant Growth: A Multidisciplinary Overview*

[11] Scott A. *et al.* (2018) *Performance of a magnesia silica cement for Martian construction, in: Earth and Space 2018: Engineering for Extreme Environments,* American Society of Civil Engineers, Reston, VA pp. 629–636.

[12] Chaboche J.L. (2003), *Damage Mechanics.* In: Milne, I., Ritchie, R.O. and Karihaloo, B., Comprehensive Structural Integrity, Volume 2. Fundamental Theories and Mechanisms of Failure.

[13] Zuo Q.H., *et al.* (2006), *A rate-dependent damage model for brittle materials based on the dominant crack.* International Journal of Solids and Structures, 43, pp. 3350-3380; , 2006.

[14] Addessio, F.L. and, Johnson, J.N. (1990), *A constitutive model for the dynamic response of brittle materials*. Journal of Applied Physics 67, 3275–3286; .

[15] Zuo, Q.H. and Dienes, J.K. (2002), *On the types of brittle failure* LA-13962-MS, Los Alamos National Laboratory Report

[16] Zuo, Q.H. and Dienes, J.K. (2005), *On the stability of penny-shaped cracks with friction: The five types of brittle behavior* International Journal of Solids and Structures 42, 1309–1326

[17] Lewis, M.W. (1991), *Investigation of a thermodynamically consistent, dynamic brittle damage constitutive model for ceramics.* Master's Thesis, Department of Mechanical Engineering, The University of New Mexico, Albuquerque, NM.

[18] Lewis, M.W. and Schreyer, H.L.(1996), *"A thermodynamically consistent description of dynamic continuum damage"* In: Davison, L., Grady, D.E., Shahinpoor, M. (Eds.), High Pressure Shock Compression of Solids II. Springer Verlag, New York, pp. 452–471.

[19] Deganis L.E. (2010), *Incorporating a Nonlinear Equation of State in a Damage Model for High Velocity Impact Analysis of Brittle Materials.* M.S. Thesis, University of Alabama in Huntsville

[20] Zhuojun Hu *et al.* (2022), *Research progress on lunar and Martian concrete*, Construction and Building Materials

[21] Heather A. Oravec *et al.* (2021), *Geotechnical Review of Existing Mars Soil Simulants for Surface Mobility*, ASCE Earth & Space Conference

[22] Kamps, O.M *et al.* (2020) *Defining Surface Types of Mars Using Global CRISM Summary Product Maps*. J. Geophys. Res. -Planets 125 Research Article 10.1029/2019JE006337

[23] Putzig, N.E., Mellon, M.T. (2007), *Apparent thermal inertia and the surface heterogeneity of Mars*. Icarus 191 (1), 68–94.

[24] Christensen, P.R., *et al.* (2003), *Morphology and composition of the surface of Mars: Mars Odyssey THEMIS results*. Science 300.

[25] Banerdt, W.B. *et al.* (2020), *Initial results from the InSight mission on Mars.* Nat. Geosci. 13, 183–189

[26] McKay D.S., Allen C.C. (1996), *Concrete – A Practical Construction Material for Mars*, Engineering, Construction, and Operations in Space 566–570.

[27] Rogers, A.D., Christensen, P.R. (2007), *Surface mineralogy of Martian low-albedo regions from MGS-TES data: implications for upper crustal evolution and surface alteration*. J. Geophys. Res. 112 (E1).

[28] Sanders, G.B., Larson, W.E. (2011), *Integration of in-situ resource utilization into lunar/Mars exploration through field analogs*. Adv. Space Res. 47 (1), 20–29.

[29] Reches, Y. (2019), *Concrete on Mars: options, challenges, and solutions for binder-based construction on the Red Planet.* Cem. Concr. Compos. 104. 103349.

[30] Pester R. (2023), *How long will it take for humans to colonize another planet?* Live Science Article

[31] Wu X. *et al.* (2012), *Early Pottery at 20,000 Years Ago in Xianrendong Cave, China*, Science VOL 336 Article

[32] *A brief history of ceramics and glass*, The American Ceramic Society online article

[33] *History of Concrete*, Irish Concrete Society online article

[34] Berto F. (2014), *Brittle or Quasi-Brittle Fracture of Engineering Materials: Recent Developments and New Challenges*, Advances in Materials Science and Engineering, Volume 2014 | Article ID 347485

[35] Roylance D. (2001), *Introduction to Fracture Mechanics*, Department of Materials Science and Engineering, Massachusetts Institute of Technology

[36] https://www.fracturemechanics.org/

[37] Kirsch, E.G. (1898), *Die Theorie der Elastizität und die Bedürfnisse der Festigkeitslehre*, Zeitschrift des Vereines deutscher Ingenieure, Vol. 42, pp. 797-807.

[38] Inglis, C.E. (1913), *Stresses in Plates Due to the Presence of Cracks and Sharp Corners*, Transactions of the Institute of Naval Architects, Vol. 55, pp. 219-241.

[39] Griffith, A.A. (1920), *The Phenomena of Rupture and Flow in Solids*, Philosophical Transactions, Series A, Vol. 221, pp. 163-198.

[40] Kwan A. and Chu S.H. (2018), *Direct tension behaviour of steel fibre reinforced concrete measured by a new test method*, Article in Engineering Structures, Vol. 176, pp. 324-336

[41] Bazant Z. (1992) *Fracture Mechanics of Concrete*

[42] Zuo, Q.H, Deganis L.E. and Wang. G. (2012), *Elastic waves and damage quantification in brittle material with evolving damage,* J. Phys. D: Appl. Phys. 45 (2012)

[43] Schreyer H.L., Chen Z. (1986), *One-Dimensional Softening with Localization,* Journal of Applied Mechanics, Vol. 53

[44] Gopalaratnam V.S. and Shah S.P. (1985), *Softening Response of Plain Concrete in Direct Tension,* American Concrete Institute (ACI) Materials Journal Vol. 82

[45] Schreyer H.L. and Zuo Q.H. (1995), *Anisotropic Yield Surfaces Based on Elastic Projection Operators*, J. Appl. Mech. Vol. 62

[46] Schreyer H.L. and Zuo Q.H. (1995), *A note on pure-longitudinal and pure-shear waves in cubic crystals*, J. Acoust. Soc. Amer. Vol. 98

[47] Zuo Q. H., Toutanji H. A. and Ueno S. (2010), *Modeling Damage in Concrete Pavements and Bridges*, UTCA Report 09301

[48] Bazant Z.P., Belytschko T.B. and Change T. (1984), *Continuum Theory for Strain-Softening*, Journal of Engineering Mechanics, Vol. 110, Issue 12

[49] Zuo Q.H., Dienes J.K., Middleditch J. and Meyer H. W. (2008), *Modeling anisotropic damage in an encapsulated ceramic under ballistic impact,* Journal of Applied Physics, Vol.104

[50] Lemaitre, J. and Chaboche, J.L. (1990), *Mechanics of solid materials,* English Translation. Cambridge University Press, New York

[51] *Yao W., Xia K., Liu H. (2018), Influence of heating on the dynamic tensile strength of two mortars: Experiments and models,* International Journal of Impact Engineering, Vol. 122

[52] Chen X. and Bu J. (2016), *Experimental Study on Direct Tensile Behavior of Concrete under Various Loading Regimes,* Technical Paper, ACI Materials Journal, Title No. 113-M46

[53] Deganis L.E. and Zuo, Q. H. (2011), *Crack-mechanics based brittle damage model including nonlinear equation of state and porosity growth*, J. Appl. Phys. Vol. 109, 073504

[54] Zuo, Q.H., Disilvestro D. and Richter J. D. (2010), *A Rate-dependent Model for Damage and Plasticity of Brittle Materials Under Dynamic Loading*, International Journal of Solids and Structures, Vol. 47, pp. 2790-2798.

[55] Muller P. *et al.* (2019), *Nasa Centennial Challenge: Three Dimensional (3D) Printed Habitat, Phase 3,* 70th International Astronautical Congress (IAC) Paper, IAC-19-E5.1.8

[56] Mondal, S., Olsen-Kettle, L.M. and Gross, L. (2020), *Regularization of continuum damage mechanics models for 3-D brittle materials using implicit gradient enhancement*, Computers and Geotechnics, Vol. 122, p.103505.

[57] De Borst, R., Sluys, L.J., Muhlhaus, H.B. and Pamin, J. (1993), *Fundamental issues in finite element analyses of localization of deformation*, Engineering computations, Vol. 10, Issue 2, pp.99-121

[58] Liu, Y., Murakami, S. and Hayakawa, K. (1993), *Mesh dependence and stress singularity in local approach to creep-crack growth analysis*, Transactions of the Japan Society of Mechanical Engineers Series A, Vol. 59, Issue 564, pp.1811-1818.

[59] Murakami, S. and Liu, Y. (1995), *Mesh-dependence in local approach to creep fracture. International Journal of Damage Mechanics*, Vol. 4, Issue 3, pp.230-250.

[60] A.B. Kunin, Q.H. Zuo (2016), *Stability and well-posedness of a rate-dependent damage model for brittle materials based on crack mechanics*, Applied Mathematical Modelling, Vol. 40, Issues 5–6, pp. 3801-3811

[61] Q.H. Zuo, D.J. Alldredge (2010) *Stability and well-posedness of a rate-dependent strain-softening plasticity model*, Int. J. Theor. Appl. Multiscale Mech. Vol 1, Issue 3, pp. 195–218

[62] Addessio, F.L., Johnson, J.N. (1993), *Rate-dependent ductile failure model*, Journal of Applied Physics Vol. 73, pp. 1640–1648.

[63] D.A. Hordijk (1991), *Local approach to fatigue of concrete*, Dissertation, Delft University of Technology